

Supplementary Materials for

Barely porous organic cages for hydrogen isotope separation

Ming Liu, Linda Zhang, Marc A. Little, Venkat Kapil, Michele Ceriotti, Siyuan Yang, Lifeng Ding, Daniel L. Holden, Rafael Balderas-Xicohténcatl, Donglin He, Rob Clowes, Samantha Y. Chong, Gisela Schütz, Linjiang Chen, Michael Hirscher*, Andrew I. Cooper*

*Corresponding author. Email: aicooper@liverpool.ac.uk (A.I.C.); hirscher@is.mpg.de (M.H.)

Published 1 November 2019, *Science* **366**, 613 (2019)
DOI: [10.1126/science.aax7427](https://doi.org/10.1126/science.aax7427)

This PDF file includes:

Materials and Methods
Supplementary Text
Figs. S1 to S44
Tables S1 to S8
References

Materials and Methods

Materials

Nomenclature: The organic cage molecules were named according to the ‘tying’ molecules molecules that were reacted with the six diamine groups of **RCC3**. Hence, **FT**, **AT**, **ET**, and **PT** represent products where the diamine group/s were tied with formaldehyde, acetone, ethanal (acetaldehyde), and propionaldehyde. The preceding number indicates how many of the **RCC3** diamine groups were reacted in this way; for example, **1AT-5FT-RCC3** is the product formed by sequentially reacting **RCC3** with one acetone molecule (**1AT**) and then five formaldehyde molecules (**5FT**).

1,3,5-Triformylbenzene was purchased from Manchester Organics, UK. All other chemicals were purchased from Sigma-Aldrich and used as received. **CC3** (covalent cage 3), **RCC3** (reduced covalent cage 3), **1AT-RCC3**, and **6FT-RCC3** were prepared according to previously reported procedures in their homochiral form, using chirally pure (1*S*,2*S*)-(+)-1,2-diaminocyclohexane (29).

Cocryst1 (CC3-S/6ET-RCC3-R Co-crystal) formation. **CC3-S** was dissolved in DCM (5 mg/mL) and added to an equivalent dichloromethane solution of **6ET-RCC3-R** at equal molar concentration (5.75 mg/mL). The solutions were mixed by direct addition at room temperature, with stirring. No precipitation was observed on mixing, but the solution became cloudy after approximately 10 minutes. The co-crystal, **Cocryst1**, was collected by filtration (Whatman® membrane filter PTFE, pore size 0.2 µm). Crystals suitable for single-crystal X-ray diffraction were cultured by vapour diffusion of acetone into the CHCl₃ solution of equal molar concentration **CC3-S** and **6ET-RCC3-R**.

Methods

1.1 Solution NMR. Solution ¹H NMR spectra were recorded at 400.13 MHz using a Bruker Avance 400 NMR spectrometer. ¹³C NMR spectra were recorded at 100.6 MHz.

1.2 Fourier Transform Infrared Spectroscopy (FTIR). IR spectra were collected on a Bruker Tensor 27 spectrometer. Samples were analyzed as KBr disks for 16 scans with a resolution of 4 cm⁻¹. Spectra were recorded in transmission mode.

1.3 Thermogravimetric Analysis. TGA analysis was carried out using a Q5000IR analyzer (TA instruments) with an automated vertical overhead thermobalance. The samples were heated at the rate of 5 °C /min.

1.4 Powder X-ray Diffraction. Laboratory powder X-ray diffraction (PXRD) patterns were collected in transmission mode on samples held on thin Mylar film in aluminium well plates on a Panalytical Empyrean diffractometer, equipped with a high throughput screening (HTS) XYZ stage, X-ray focusing mirror, and PIXcel detector, using Cu-Kα ($\lambda = 1.541 \text{ \AA}$) radiation. PXRD patterns were measured over the 2θ range 5–50°, in ~0.013° steps, over 1 hour. For indexing, samples were loaded into borosilicate glass capillaries, and PXRD patterns were recorded in transmission mode on a Panalytical Empyrean diffractometer, equipped with a sample spinner to

improve powder averaging. High resolution synchrotron PXRD data for **Cocryst1**, (CC3-S/6ET-RCC3-R), was collected using the I11 beamline at Diamond Light Source ($\lambda = 0.825015 \text{ \AA}$), which is equipped with a Mythen II position sensitive detector. This sample was loaded in a borosilicate glass capillary that was rocked to improve powder averaging during data acquisition.

1.5 Electron Microscopy. Imaging of the crystal morphology was achieved using a Hitachi S-4800 cold field emission scanning electron microscope (FE-SEM) operating in both scanning and transmission modes. Scanning-mode samples were prepared by depositing dry crystals on 15 mm Hitachi M4 aluminum stubs using an adhesive high-purity carbon tab before coating with a 2 nm layer of gold using an Emitech K550X automated sputter coater. Imaging was conducted at a working distance of 8 mm and a working voltage of 3 kV using a mix of upper and lower secondary electron detectors. Transmission-mode samples were prepared by dispersing the cage particles in a methanol suspension and depositing onto carbon-coated copper grids (300 mesh), imaging at 30 kV working voltage and 7 mm distance.

1.6 Gas Sorption Analysis. For determining gas sorption isotherms gasses of the following purities were used: hydrogen (99.9995% - BOC gases) and carbon dioxide (SCF grade – BOC gases). Surface areas and pore size distributions were measured by nitrogen adsorption and desorption at 77.3 K using a Micromeritics ASAP 2020 volumetric adsorption analyzer. Samples were degassed at offline at 80 °C for 15 h under vacuum (10⁻⁵ bar) before analysis, followed by degassing on the analysis port under vacuum, also at 80 °C. Carbon dioxide isotherms were measured at 289K using a Micromeritics 2420 volumetric adsorption analyzer using the same degassing procedure.

1.7 Single Crystal X-ray Diffraction. Single crystal X-ray data sets were measured using a Rigaku MicroMax-007 HF rotating anode diffractometer (Mo-K α radiation, $\lambda = 0.71073 \text{ \AA}$, Kappa 4-circle goniometer, Rigaku Saturn724+ detector); at beamline 11.3.1, Advanced Light Source, Berkeley, USA, using silicon monochromated synchrotron radiation ($\lambda = 0.7749 \text{ \AA}$ or 1.0332 \AA , PHOTON100 CMOS detector); or at beamline I19, Diamond Light Source, Didcot, UK using silicon double crystal monochromated synchrotron radiation ($\lambda = 0.6889 \text{ \AA}$, Dectris Pilatus 2M detector). Unless stated in the refinement details section, desolvated single crystals, which had been activated by removing solvent at 353 K under dynamic vacuum, were mounted on a MiTeGen loops and flash cooled to 100 K under a dry nitrogen gas flow. Empirical absorption corrections, using the multi-scan method, were performed with the program SADABS.(47) For synchrotron X-ray data collected at Diamond Light Source ($\lambda = 0.6889 \text{ \AA}$), data reduction and absorption corrections were performed with xia2.(48) Structures were solved with SHELXT (49) and refined by full-matrix least squares on $|F|^2$ by SHELX (50), interfaced through the programme OLEX2 (51). Unless stated all non-H-atoms were refined anisotropically, and unless stated H-atoms were fixed in geometrically estimated positions and refined using the riding model. Supplementary CIF's, which include structure factors, are available free of charge from the Cambridge Crystallographic Data Centre (CCDC) via www.ccdc.cam.ac.uk/data_request/cif.

1.8 Hydrogen isotope adsorption/separation measurements

A fully automated Sierverts apparatus iQ2 (Quantachrome Instruments) was used to perform the adsorption experiments. The calibration cell is an empty analysis carried out at the same temperature and pressure range than each experiment; corrections related the sample volume and the non-linearity of the adsorbate are made. Around 20 mg of sample were activated at 343K under vacuum for 5hrs in order to remove any solvent molecules. A coupled cryocooler based on the Gifford-McMahon cycle was used to control the sample temperature. The cooling system allows us to measure temperatures from 20 to 300K with an estimated error of < 0.05 K.

The selective adsorption after exposure to D₂/H₂ isotope mixtures was directly measured by the in-house designed setup of thermal desorption spectroscopy (TDS). For a typical process, about 4 mg sample was loaded in the sample holder and activated at 343 K under vacuum for 5 h. Then, an equimolar D₂/H₂ isotope mixture was loaded on the sample at a fixed temperature (exposure temperature, T_{exp}) for a chosen exposure time (t_{exp}). The free gas was evacuated and then the sample was cooled down to 20 K in order to preserve the adsorbed state. Finally, during heating from 20 K to room temperature with a heating rate of 0.1 K/s, the desorbing gas was continuously detected using a mass spectrometer (QMS), recognizing a pressure increase in the sample chamber when gas desorbs. The area under the desorption peak was proportional to the desorbing amount of gas, which can be quantified after careful calibration of the TDS apparatus.

1.9 Calibration of the mass spectrometer signal

A solid polycrystalline piece of a diluted Pd alloy Pd₉₅Ce₅ (~0.5 g) was used for calibration. Prior to the calibration, the alloy was etched with aqua regia in order to remove the oxide layer and it was then heated up to 600 K under high vacuum to remove any hydrogen that might be absorbed during the etching procedure. Afterwards, it was weighted and inserted into the sample chamber. At 350 K, it was loaded with 40 mbar pure H₂ or pure D₂ for 1.5–2.5 h. As H and D were bound preferentially to the Cerium atoms at low loading pressures in this diluted alloy, the alloy could be handled under ambient conditions for a short period of time. After loading, the alloy was cooled to room temperature and weighed. Afterwards, it was placed back in the sample chamber and a normal TDS measurement with 0.1 K/s was performed. After the desorption, the alloy was cooled back to RT and weighted again. The weight difference between unloaded state and loaded state was equal to the mass uptake of hydrogen or deuterium, respectively.

Supplementary Text

2.1 Single-crystal-to-single-crystal reaction of **1AT-RCC3**

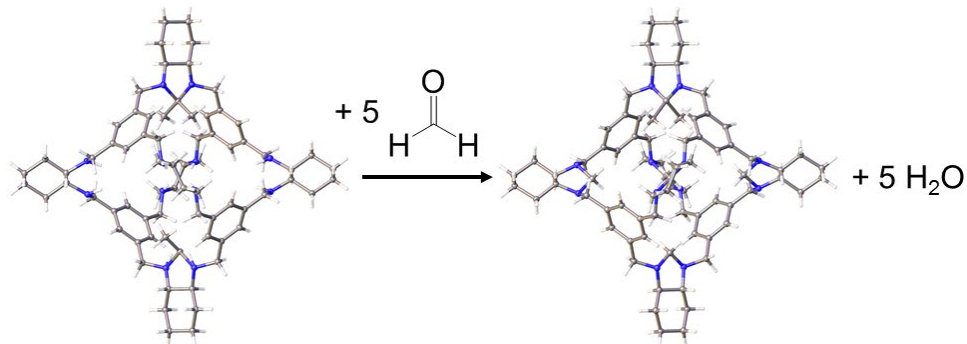


Fig. S1. Single-crystal-to-single-crystal reaction of **1AT-RCC3 ($a = 25.4685(14)$ Å, $V = 16520.0(16)$ Å³ @ 100 K) to form **1AT-5FT-RCC3** ($a = 25.327(2)$ Å, $V = 16246(5)$ Å³, after removal of H₂O and residual formaldehyde under dynamic vacuum). In the crystal structure of **1AT-5FT-RCC3**, electron density between the diamine groups correlates with the formation of five methylene bridged aminal rings. There is also a small decrease in the cavity volume of the cage molecule during this solid-state reaction, indicating the five additional methylene bridged aminal rings constrict the vicinal diamine groups of the parent cage.**

2.2 1AT-RCC3 - reaction with formaldehyde in solution

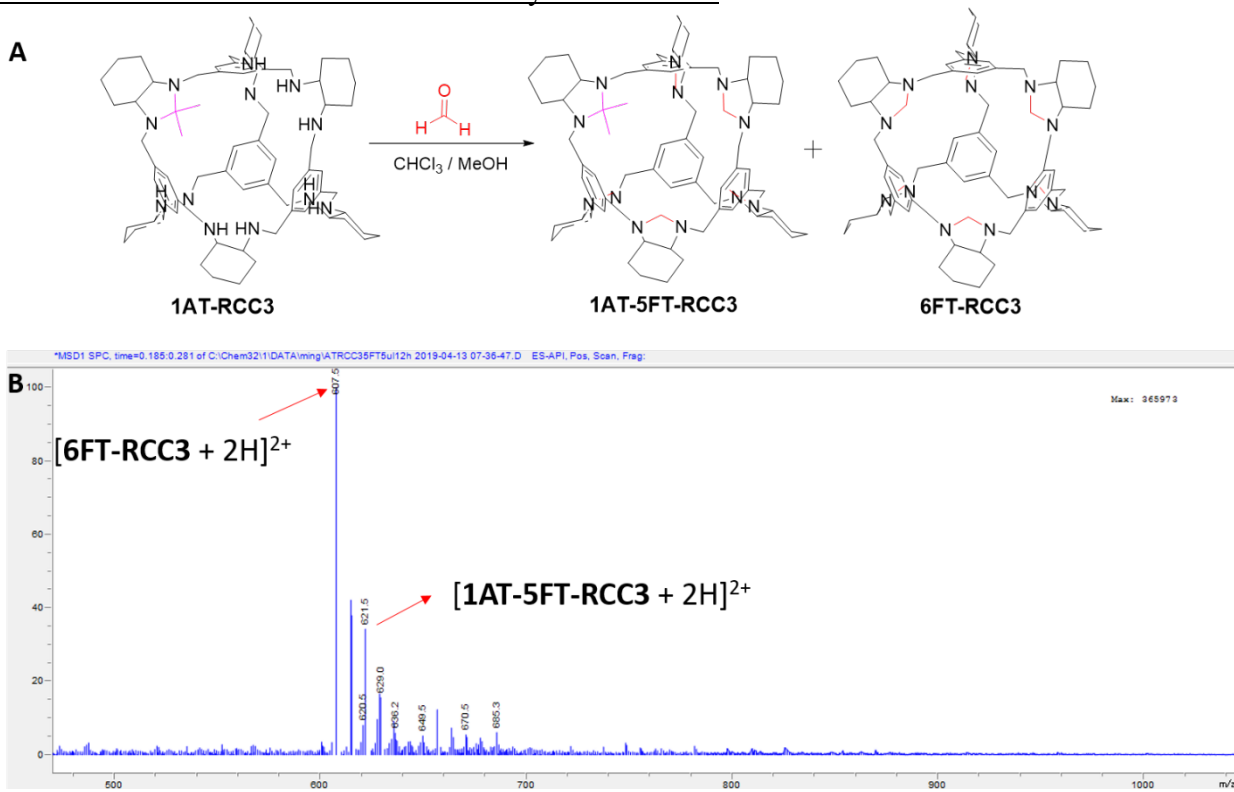


Fig. S2. 1AT-RCC3 reactions with formaldehyde in solution. A. Reaction scheme for 1AT-RCC3 and formaldehyde in solution ($\text{CHCl}_3/\text{MeOH}$, $v/v = 1:1$). B. Mass spectrum of the reaction mixture after 12 hour suggests the dominant presence of 6FT-RCC3. Signal at $m/z = 607.5$ was observed and was attributed to $[\text{6FT-RCC3} + 2\text{H}^+]^{2+}$, and the signal $m/z = 621.5$ was attributed to $[\text{1AT-5FT} + 2\text{H}^+]^{2+}$.

2.3 RCC3 - reaction with formaldehyde (5 equiv) in solution

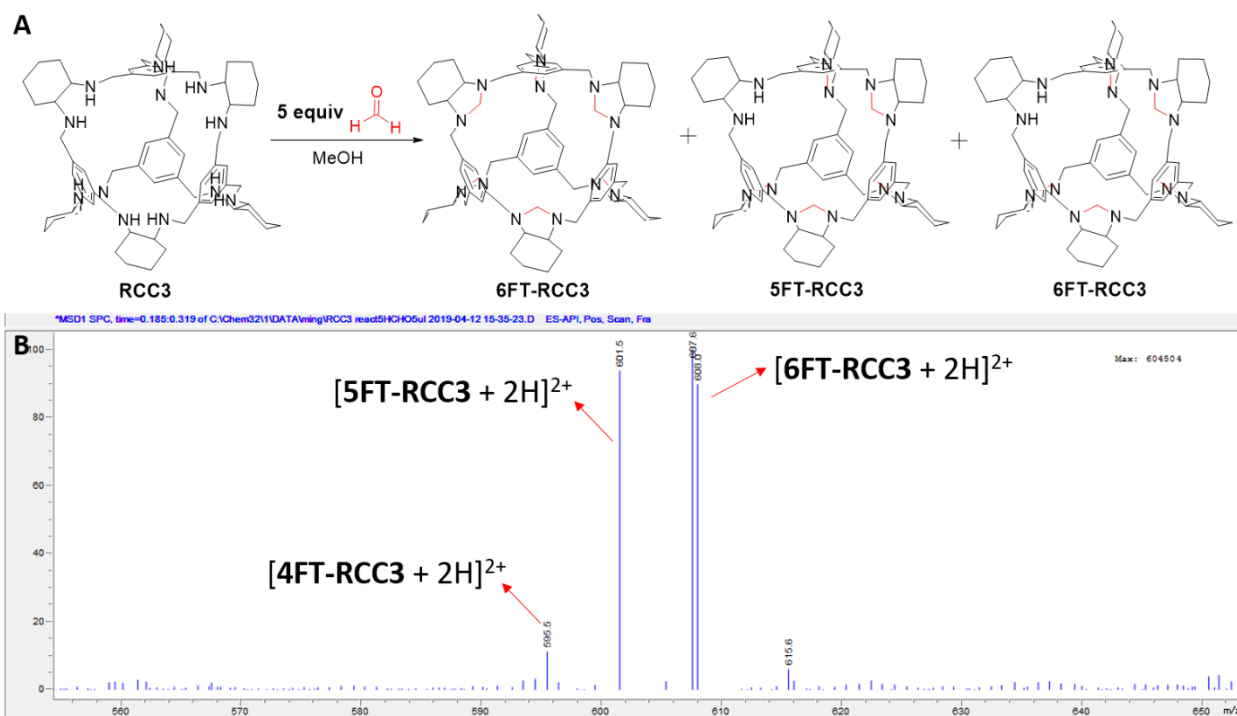


Fig. S3. Synthesis of 5FT-RCC3 by directly reacting RCC3 with formaldehyde in solution.
A. Reaction scheme for **5FT-RCC3** reacting with 5 equivalents formaldehyde in methanol. **B.** Mass spectrum of the product mixture. From the reaction, white precipitate was formed approximately 1 minute after mixing the two reactants. This precipitate was collected by filtration after 5mins and the filtrate was analysed by MS. The main products, based on their m/z peaks, were determined to be: **4FT-RCC3**, **5FT-RCC3** and **6FT-RCC3**.

2.4 Crystallographic analysis of the isostructural cages

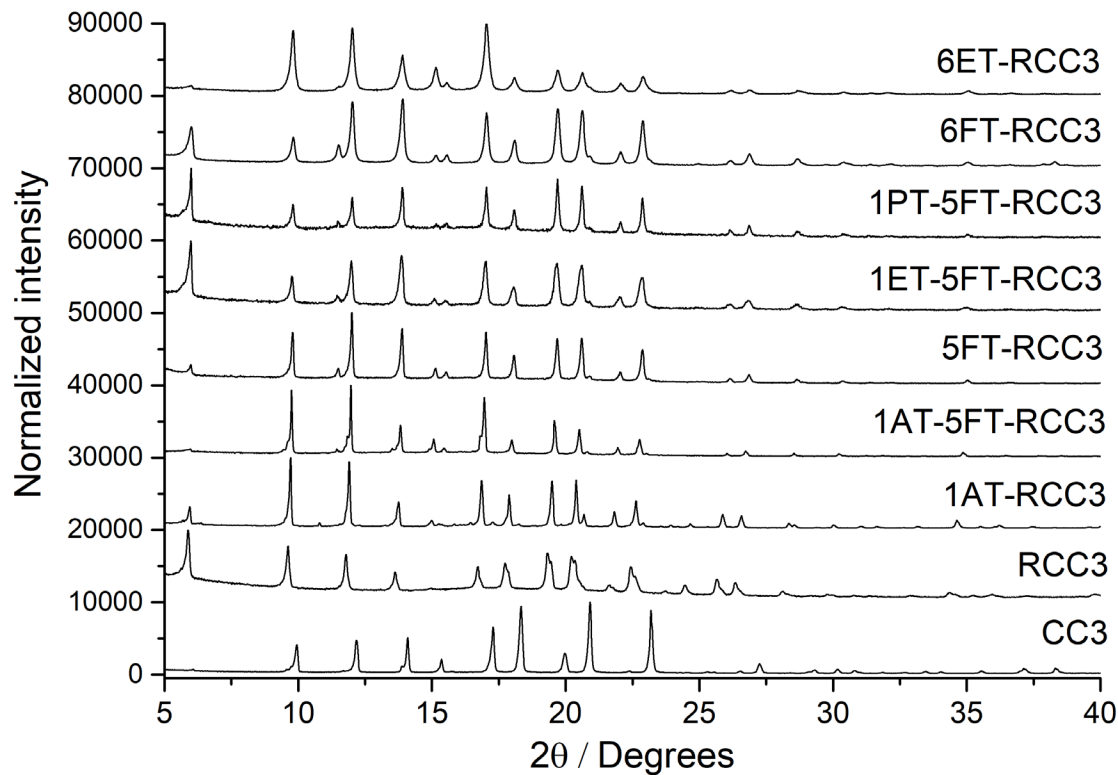


Fig. S4. Experimental PXRD patterns (Cu-K α) of the isostructural cages, as synthesized.

Table S1. Unit cell parameters and cavity volume calculations for RT cage series. All x-ray data sets were recorded at 100 K after activating the crystals pores under dynamic vacuum at 353 K.

	RCC3 ^[a]	1AT-RCC3 ^[a]	1AT-5FT-RCC3	6FT-RCC3 ^[a]	5FT-RCC3	1ET-5FT-RCC3	1PT-5FT-RCC3	6ET-RCC3
a (Å)	25.711	25.469	25.318	25.316	25.261	25.252	25.220	25.216
V (Å³)	16999	16520	16228	16225	16120	16102	16041	16033
Cavity volume (Å³)^[b]	186.9	127.3	91.7	129.6	140.1	97.3	95.8	29.5

[a] Previously reported unit cell parameters (29). [b] Calculated using VO/DOO, probe radius = 2.0 Å (43).

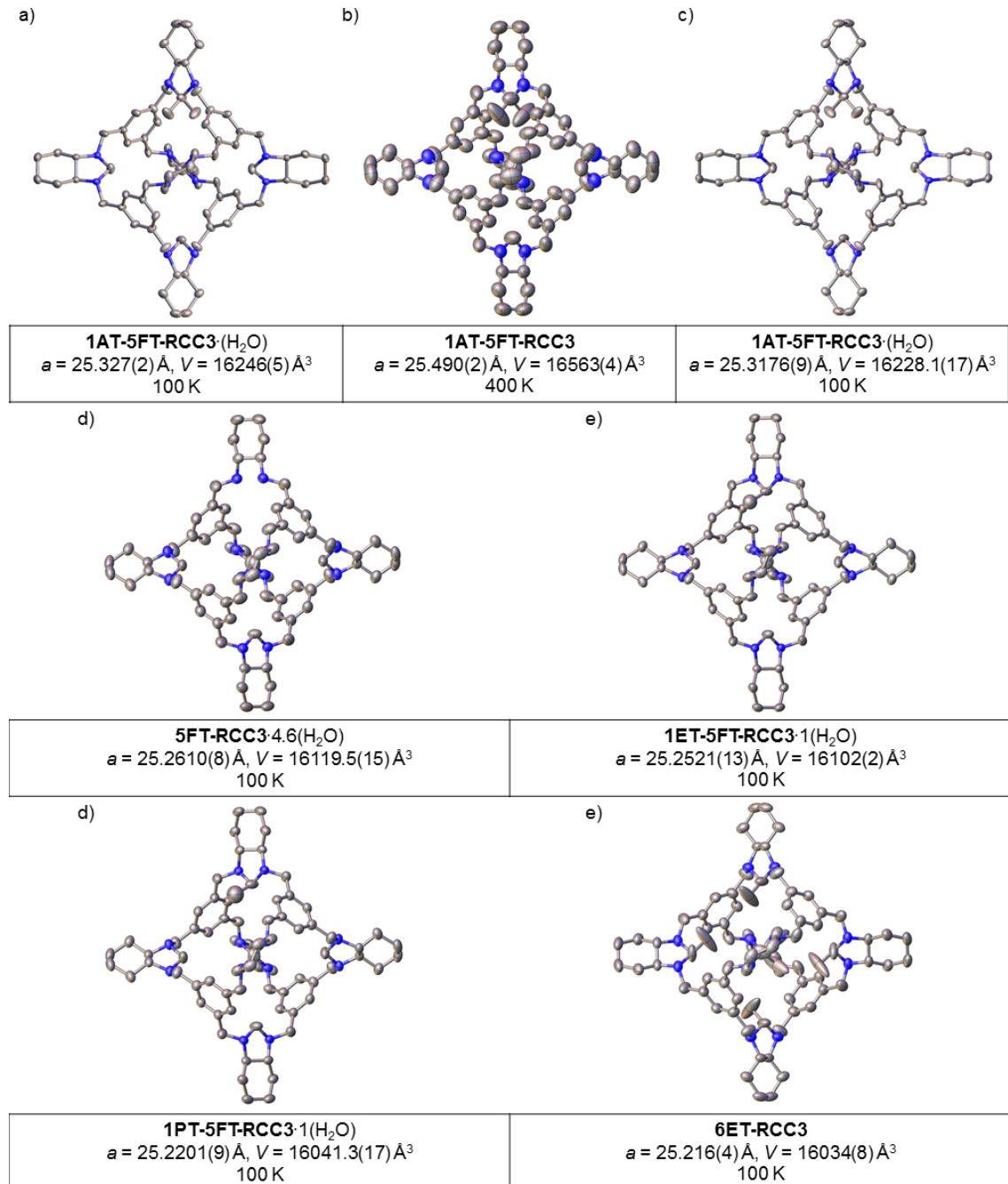


Fig. S5. Displacement ellipsoid plots from the single crystal structures of the single component cage crystals. All the structures were refined in the chiral cubic space group $F\bar{4}_132$; disordered residual H_2O and all H-atoms are omitted for clarity; ellipsoids are displayed at 50% probability level. The single crystal structure of **1AT-5FT-RCC3** was recorded at 100 K (a) and 400 K (b), after exposing a single crystal of **1AT-RCC3** to formaldehyde vapor at RT for 12 hours and then degassing the single crystals at 363 K under dynamic vacuum. (c) This phase of **1AT-5FT-RCC3** could also be isolated after recrystallising this cage from $\text{CH}_2\text{Cl}_2/\text{acetone}$. Single crystal structures of **5FT-RCC3·4.6(H₂O)** (d); **1ET-5FT-RCC3·(H₂O)** (e); **1PT-5FT-RCC3·(H₂O)** (f); and **6ET-RCC3** (g), were recorded using synchrotron radiation. For full refinement detail, see Supplementary Section 2.7 and tables S5-S7.

2.5 Xe and Kr sorption analysis of 1AT-5FT-RCC3

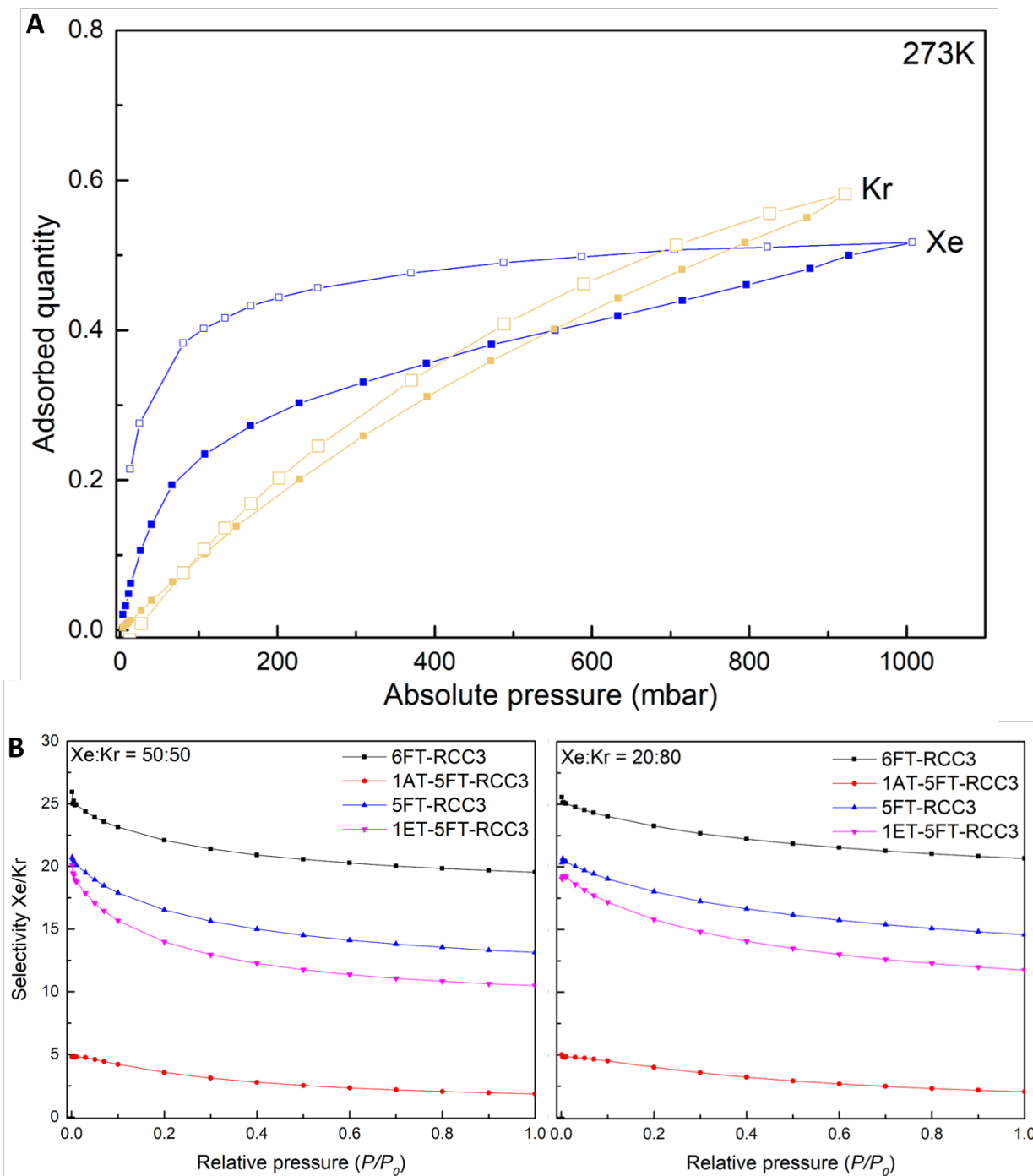


Fig. S6. **A.** Experimental Xe and Kr isotherms for **1AT-5FT-RCC3** recorded at 273 K. At a pressure 800 mbar and above, **1AT-5FT-RCC3** adsorbs more Kr than Xe. **B.** IAST plots showing that the Xe/Kr selectivity can be tuned using the isostructural cages.

2.6 Hydrogen isotope isotherms of **6ET-RCC3**, **6FT-RCC3** and **CC3**

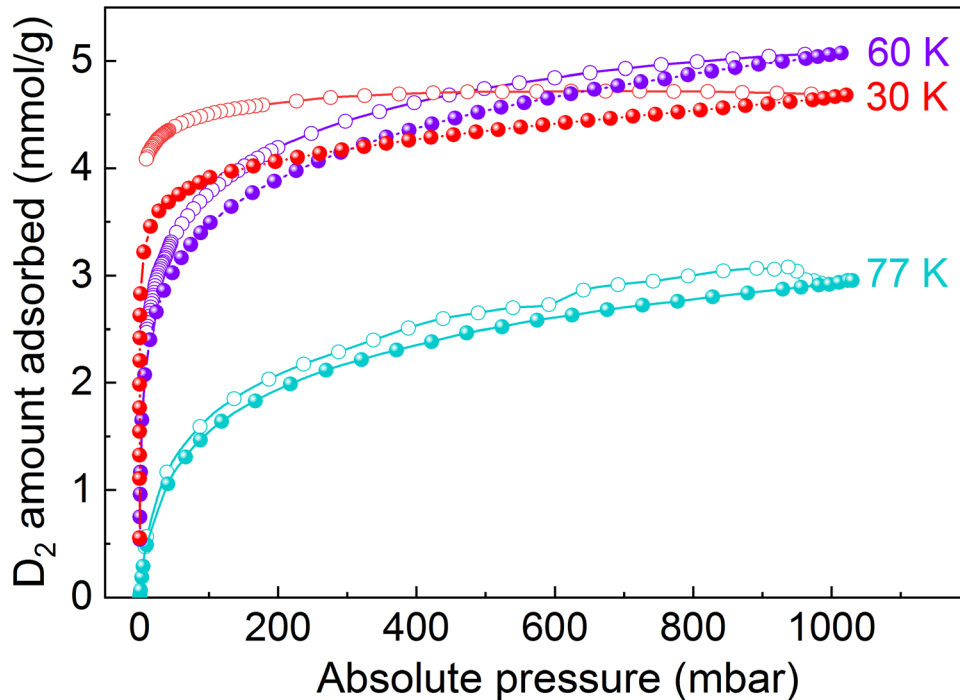


Fig. S7. Deuterium adsorption (closed) and desorption (open) isotherms of **6ET-RCC3** at different temperatures (equilibrium time 100 h).

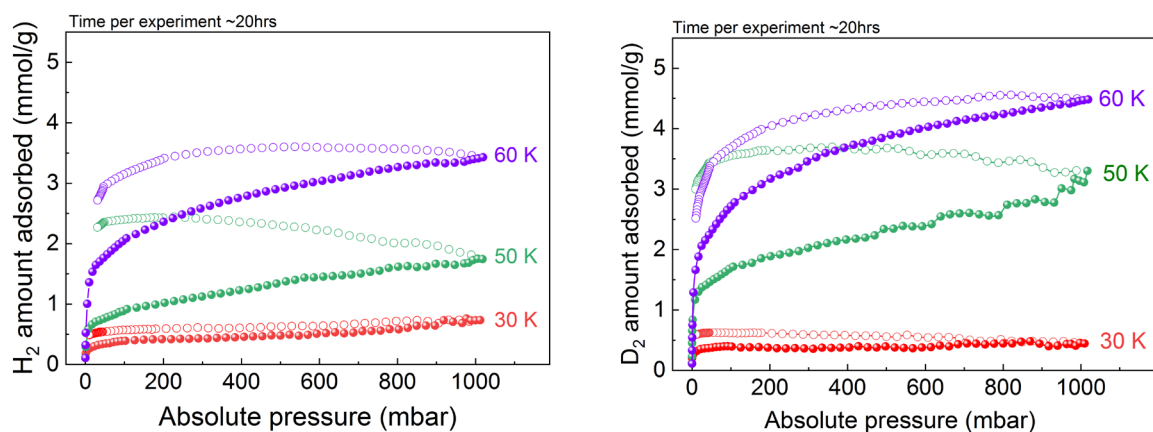


Fig. S8. H_2 (left) and D_2 (right) adsorption (closed) and desorption (open) isotherms of **6ET-RCC3** at different temperatures (equilibrium time 20 h).

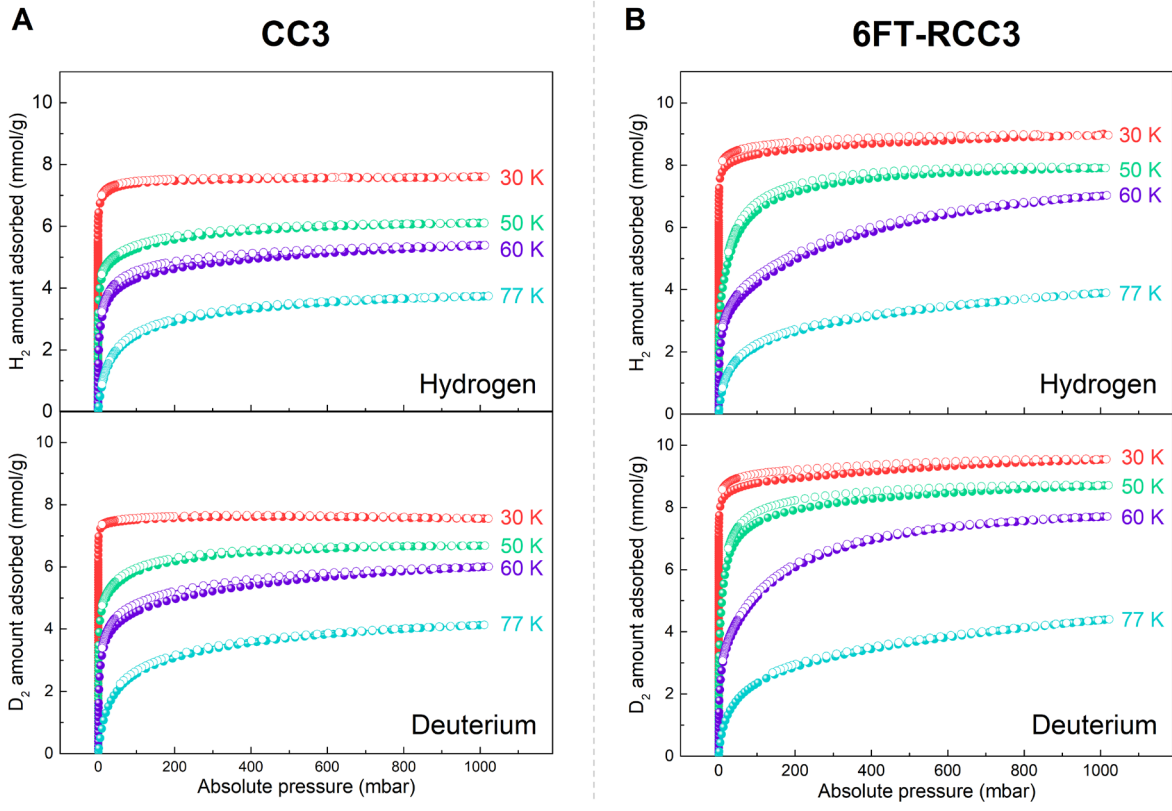
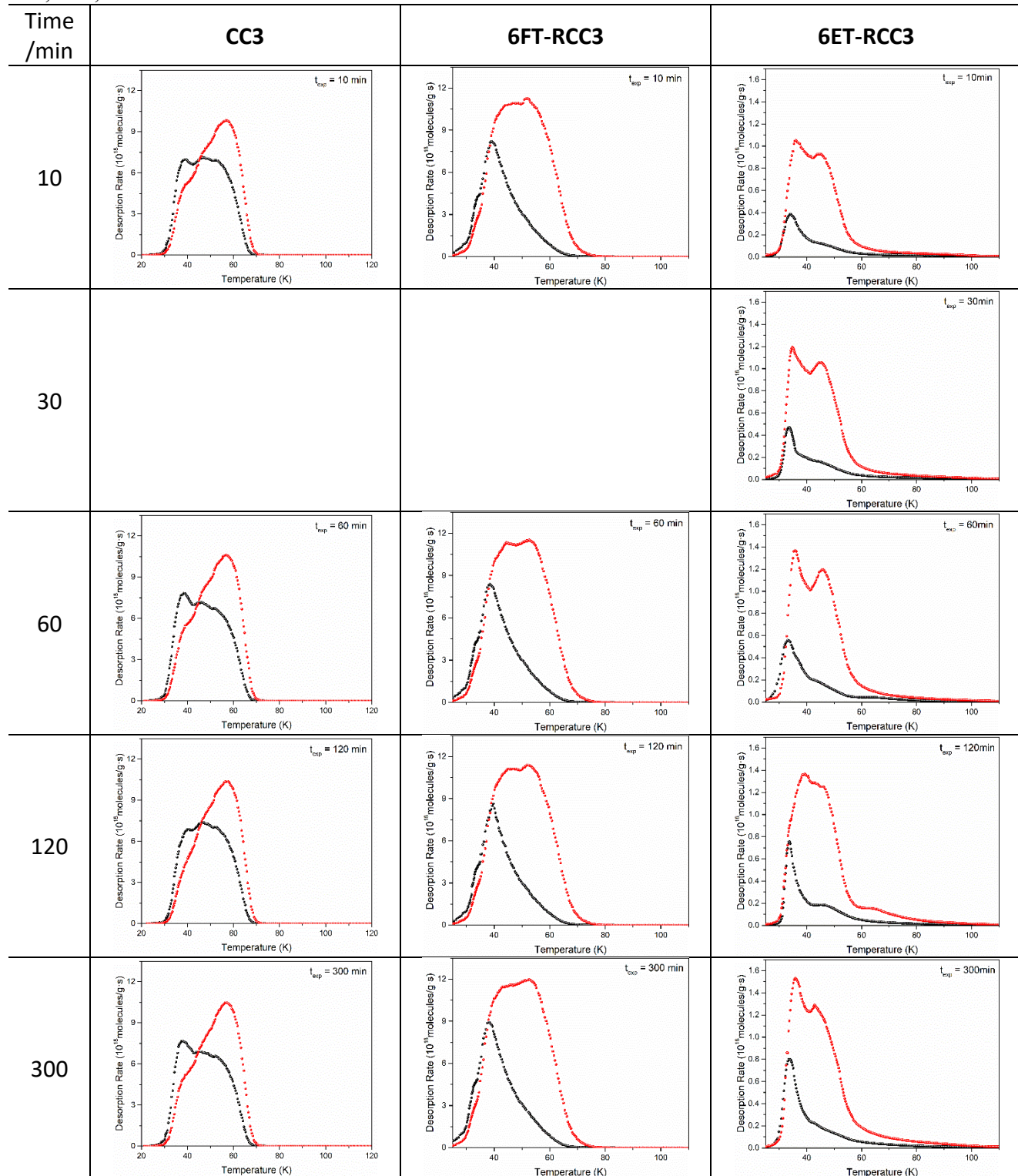


Fig. S9. Hydrogen (upper) and Deuterium (bottom) adsorption (closed) and desorption (open) isotherms of (A) CC3 and (B) 6FT-RCC3 at different temperatures.

Table S2. H₂ (black) and D₂ (red) thermal desorption spectra of 10 mbar 1:1 H₂/D₂ isotope mixture on CC3, 6FT-RCC3, and 6ET-RCC3 at 30 K for various exposure time (t_{exp}): 10, 30, 60, 120, and 300 min.



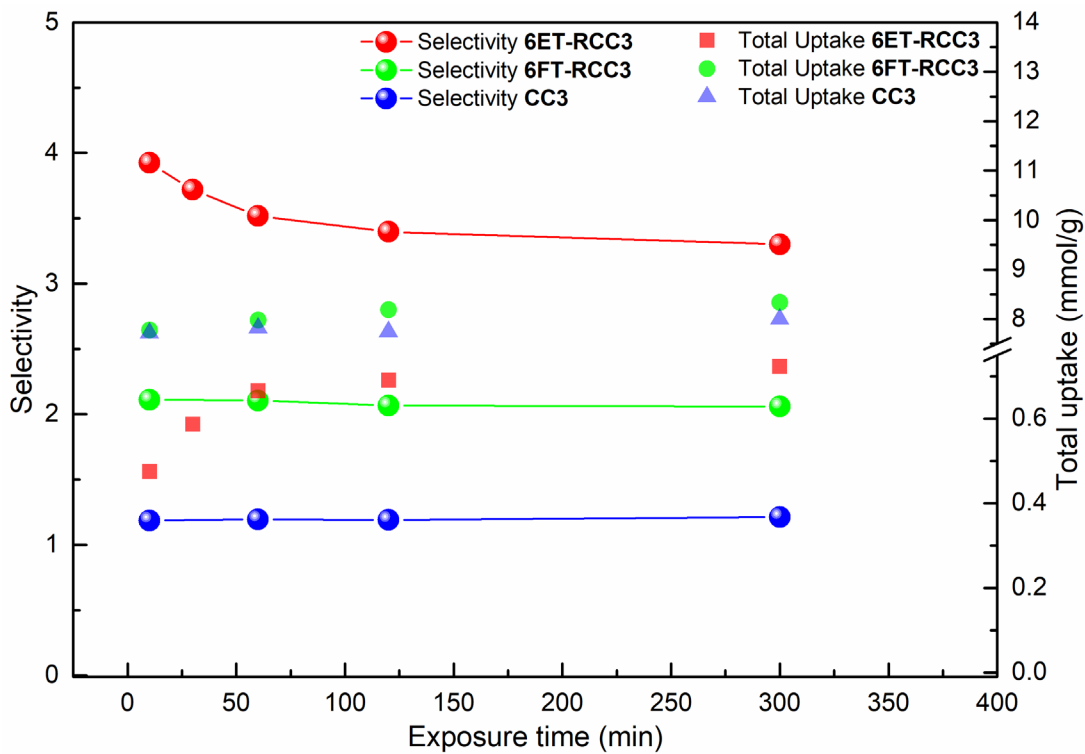


Fig. S10. D_2/H_2 selectivities and gas uptakes as function of exposure time at 30 K for **CC3**, **6FT-RCC3**, and **6ET-RCC3**.

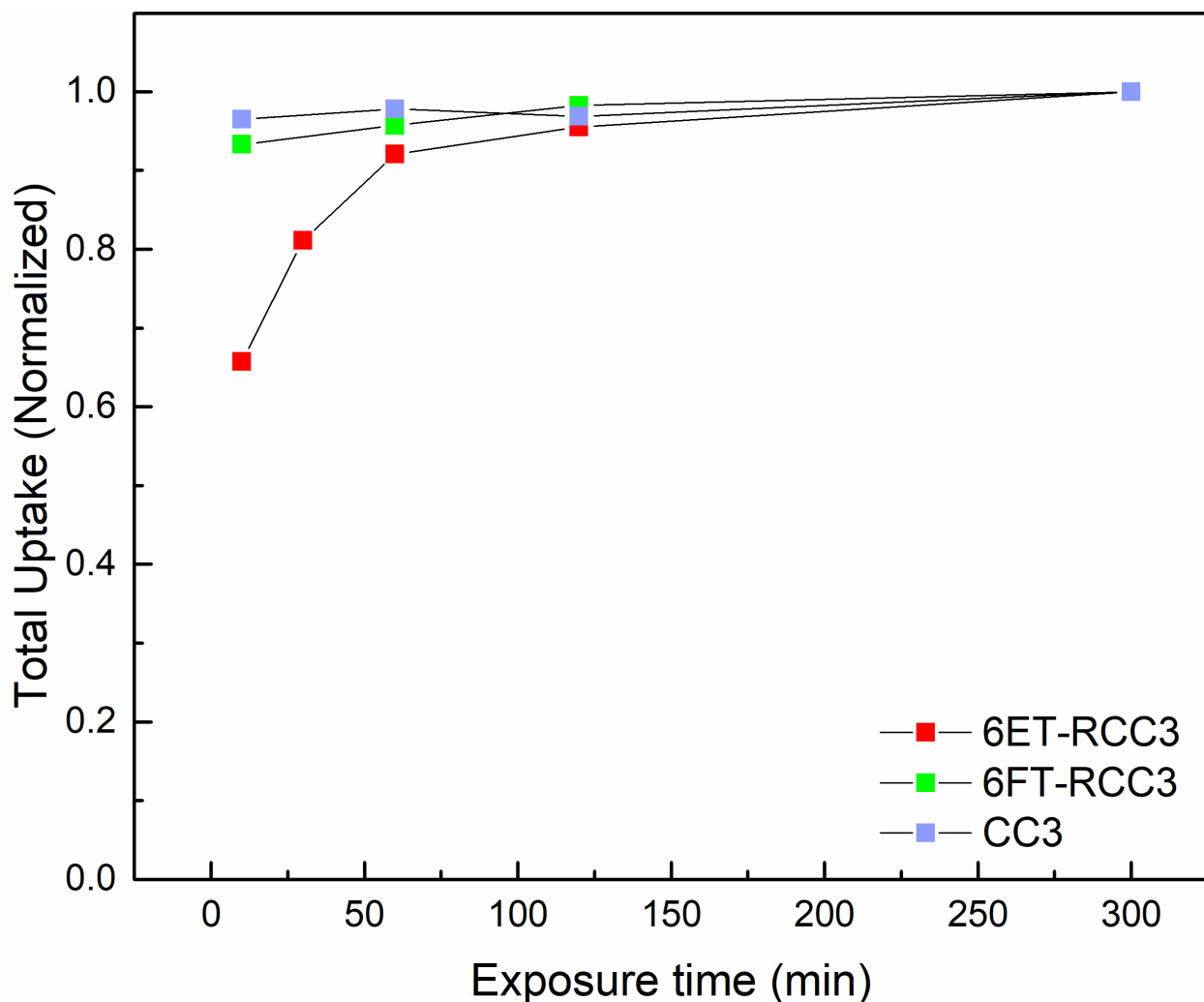


Fig. S11. Normalized gas uptakes as function of exposure time at 30 K for **CC3**, **6FT-RCC3**, and **6ET-RCC3**.

2.7 Structure analysis, hydrogen isotopes isotherms and TDS studies of Cocryst1

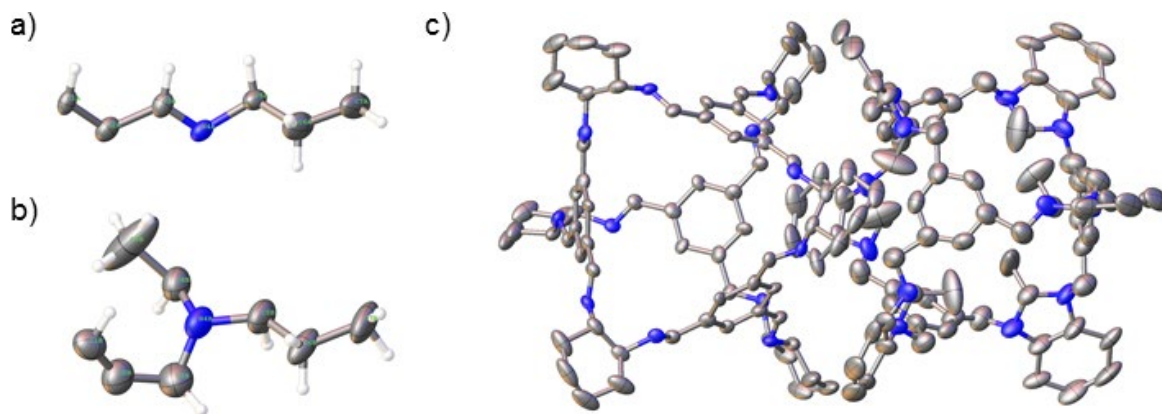


Fig. S12. Displacement ellipsoid plots from the single crystal structure, **Cocryst1 (CC3-S, 6ET-RCC3-R)**, showing the asymmetric units of **CC3-S** (a) and **6ET-RCC3-R** (b). The crystal structure was refined in the chiral cubic space group $F\bar{4}32$, and in the structure the -R and -S cage molecules are disordered over one position. Both cages were refined with site occupancies of 50%, based on NMR characterization, and the idealized window-to-window packing of **CC3-S** and **6ET-RCC3-R** cages is shown in (c). Due to the crystallographic symmetry, we could not determine how much of the crystal this idealized packing arrangement of cages extends over. Previously, we have reported that this perfect packing arrangement of -R and -S cages can drop the crystallographic symmetry of related cocrystals to $F23$, and that the -R and -S cages are ordered in the crystal lattices of these single crystal structures. (34, 52) By contrast, when we refined **Cocryst1** in the space group $F23$, we still observed disorder.

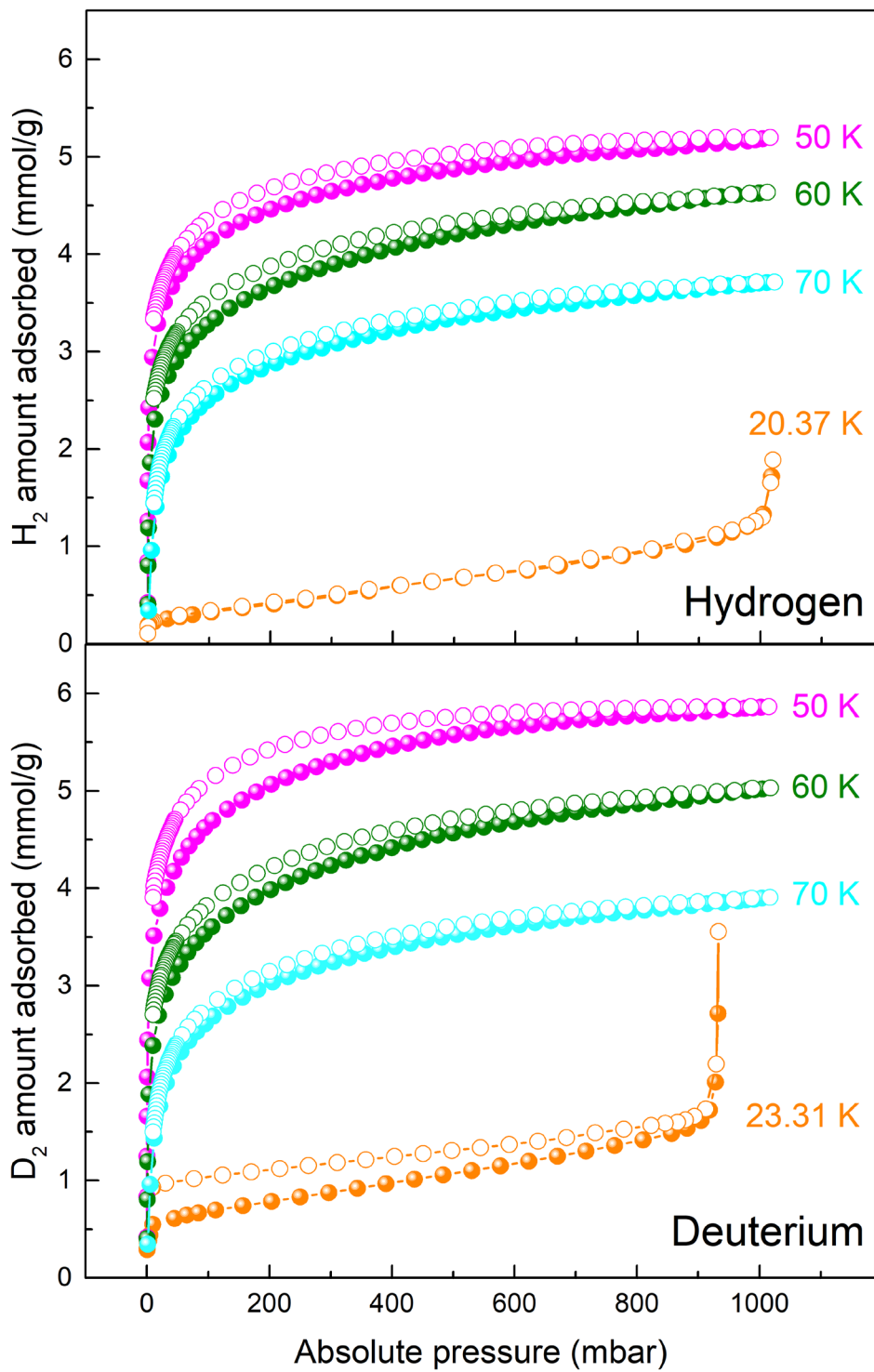


Fig. S13. Hydrogen (upper) and Deuterium (bottom) adsorption (closed) and desorption (open) isotherms of the **CoCryst1** at different temperatures.

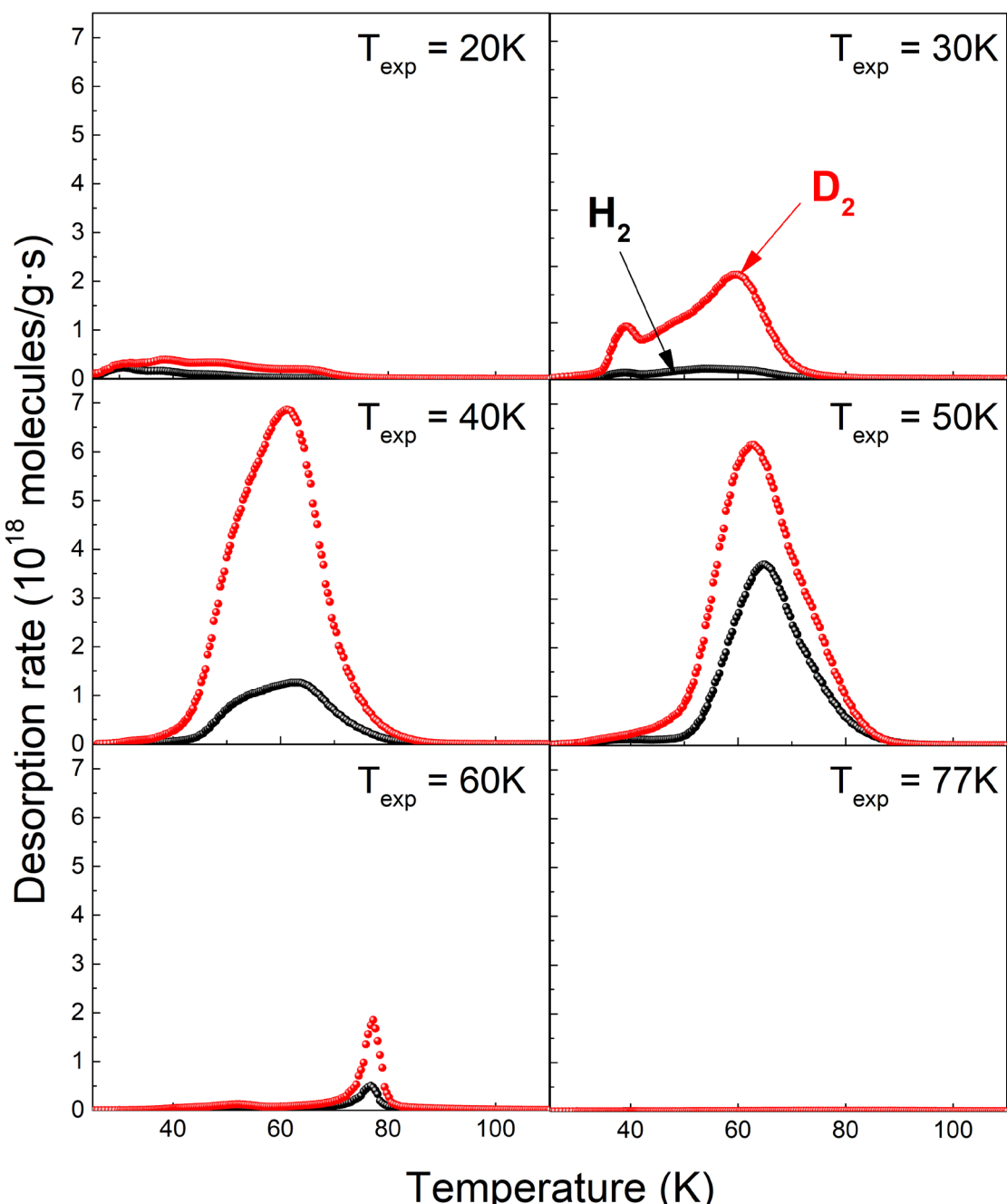


Fig. S14. Thermal desorption spectra (TDS) of **Cocryst1** obtained after exposure to a 10 mbar 1:1 D_2/H_2 isotope mixture at different exposure temperatures for a fixed exposure time of 30 min. The desorption spectra after evacuation at exposure temperature were measured for a heating rate of 0.1 K/s.

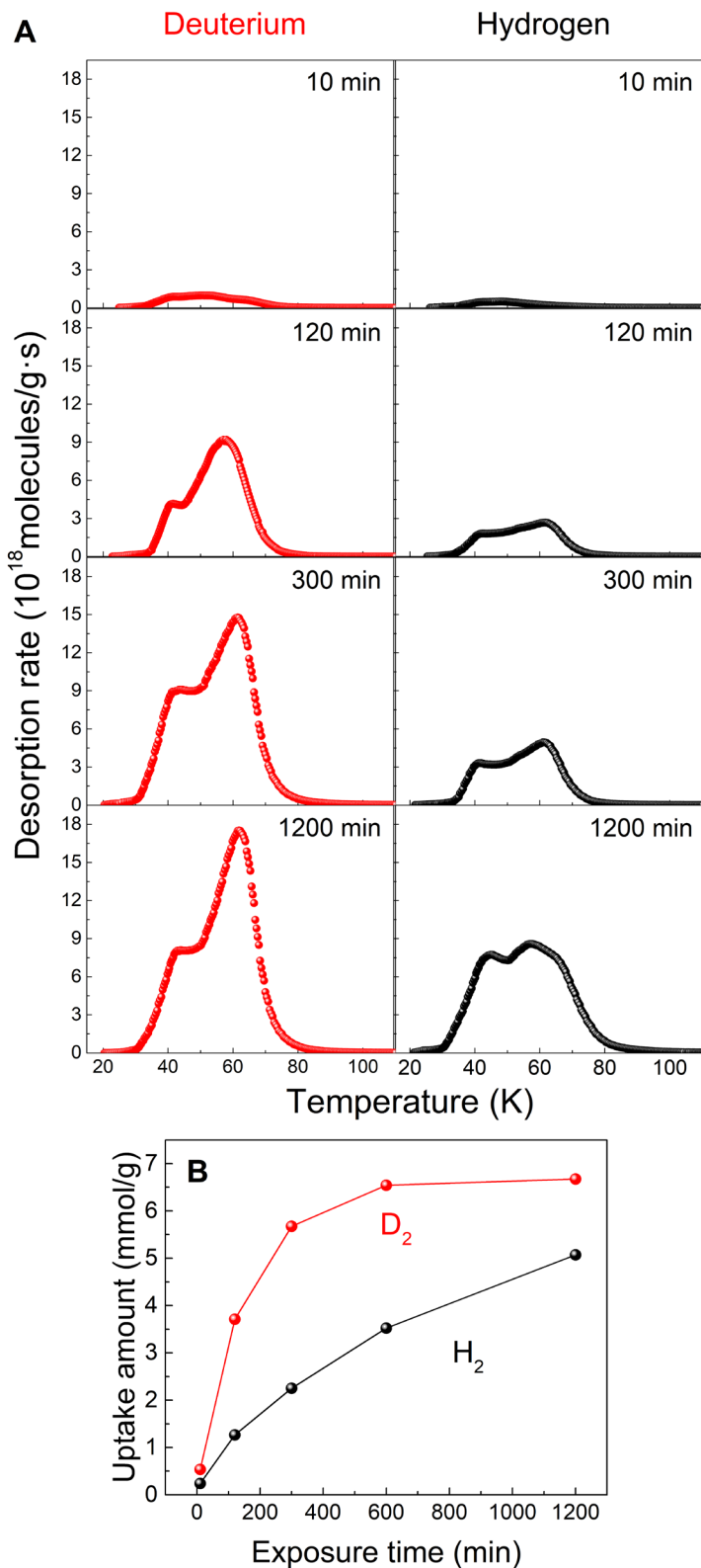


Fig. S15. (A) Deuterium (red) and hydrogen (black) desorption spectra obtained for different exposure time. **Cocryst1** is exposed to 10 mbar pure gas separately at 30 K; (B) The corresponding amount of adsorbed H_2 (black), D_2 (red) pure gas as functions of exposure time.

Table S3. Summary of hydrogen isotope selectivities and adsorption amount for various porous materials via KQS (directly measured by TDS).

Compound	T _{exp} (K)	Selectivity (D ₂ /H ₂) (1:1 Mixture)	Adsorbed D ₂ amount (mmol/g)	Ref.
MFU-4 (Co, Cl)	30	4.0	4.72	(44)
	40	2.0	4.66	
MFU-4 (Zn, Cl)	40	6.9	0.02	(6)
	50	5.8	0.40	
	60	7.5	1.24	
MFU-4 (Zn, Br)	70	2.1	0.07	(44)
MFU-4I	40	1.7	8.30	(22)
Takeda 3A	40	6.8	0.01	(44)
	50	5.9	0.03	
MOF-5	70	1.4	11.15	
Py@COF-1	22	9.7	0.50	(46)
	30	7.9	0.60	
IFP-1	30	2.0	9.30	
IFP-3	30	2.8	2.49	(45)
IFP-7	77	1.5	0.05	
IFP-4	77	2.1	0.01	
Zeolite 5A	30	2.7	4	(16)
CC3	30	1.7	3.67	
	50	1.8	1.20	
6FT-RCC3	30	2.2	2.81	This work
	50	3.0	0.78	
6ET-RCC3	30	3.9	0.39	
	50	1.8	0.32	
Cocryst1	30	8.0	4.72	

Table S4. Summary of experimentally measured hydrogen isotope separation performance on various porous materials via KQS.

Compound	Aperture (Å)	T (K)	P (mbar)	Selectivity (D ₂ /H ₂) (1:1 Mixture)	Ratio (nD ₂ /nH ₂) (Pure Gas Isotherms)	Ratio (kD ₂ /kH ₂) (Rate constant)	Ref.	
Breakthrough								
CMS	5-7/ 15-35	77	4000	1.53 (H ₂ :D ₂ =139:175)	-	-	(53)	
Zeolite 5A	5	77		1.8 (H ₂ :D ₂ =99:1)	-	-	(54)	
Zeolite 13X	8	77		1.9 (H ₂ :D ₂ =99:1)	-	-		
Zeolite Y	6-7	77	4000	Up to 1.52 (H ₂ :D ₂ =139:175)	-	-	(55)	
Pure gas sorption								
CMS T3A	5.46	77	5-1000	-	1.063	-	(56)	
PCS	5.66	77	50-500	-	-	Up to 1.9		
		77	5-1000	-	1.097	-		
		77	0-50	-	-	Up to 1.25		
3KT-172	4.9	77	20	-	-	1.86	(57)	
1.5GN-H	4.6	77	100	-	-	5.83		
CNH	-	77	70-1000	-	1.09	-	(58)	
HKUST-1	9/5	77	20	-	1.23	-		
SWCNT	13-14	77	10000	-	1.2	-	(59)	
SG-SWCNT	28.5	40	0.1-10	Up to 5*	-	-	(60)	
		77		Up to 3.8*	-	-		
LA-SWCNT	13.7	40	0.1-10	Up to 2.8*	-	-		
		77		Up to 1.5*	-	-		
Zeolite 5A	5	77	0.01-10	Up to 3.26*	-	-	(61)	
Zeolite NaX	7.4	77	139	-	1.18	-	(62)	
		30	Stand- ard pressure	-	1.06	-		
		40			1.03			
		50			1.43			
		77			1.33			
Zeolite 4A	4	77	150	2.09*	-	-	(63)	
Zeolite 5A	5	77	150	2.48*	-	-		
Zeolite Y	6-7	77	150	1.32*	-	-		
Zeolite 10X	8	77	150	1.3*	-	-		
CMK-3	35	77	150	0.95*	-	-	(64)	
Zeolite 13X	8	77	0.1-1000	Up to 3.2*	-	-		
CuBOTf	2×2 8.7×8.7	40	0.1-10	Up to 5.8*	-	-		
		77	0.1-10	Up to 5.8*	-	-	(33)	
		77	50-1000	-	1.13	-		

M' MOF 1	5.6×12	77 87	5-1000	- -	1.09 1.11	- -	(19)
ZIF-7	3	20	Near-zero pressure	-	-	-	(20)
ZIF-8	3.4	20		-	11	-	
COF-1	9	20		-	7	-	
COF-102	12	20		-	1	-	
MFU-4 (Zn)	3.88/ 11.93/ 2.52	50 60 70	7	-	4.1	-	(6)
			4	-	2.3	-	
			1.8	-	1.7	-	
Fe-MOF-74	11	77	Near-zero pressure	2.5*	2.5	-	(35)
Co-MOF-74	11	77		3.2*	3.25	-	
Ni-MOF-74	11	77		5*	4.5	-	
VSB-5	11	140	0-1000	Up to 4*	-	-	(65)
12-Connected MOFs	10	77	1000	-	1.1	-	(66)
Cu2L2	7.3	77	100	-	1.2	-	(67)

Pseudoisobaric mixture gas sorption(8)

Zeolite 3A	3	77-130	85	4.33	-	-	(68)
		77-140		3.04	-	-	
		77-160		2.32	-	-	
		77-130	58	3.19*	-	-	
		77-140		2.60*	-	-	
		77-160		2.20*	-	-	
MS13X	8.6	77	-	3.05	-	-	(69)

* D₂/H₂ mixture selectivity calculated by IAST

2.8 Additional Single Crystal and Powder X-ray Diffraction Details

For full single crystal refinement details, see Tables S5-S7, and for further refinement details about the restraint used during refinement see the text below and the Supporting CIF files.

1AT-5FT-RCC3: In the three crystal structures of **1AT-5FT-RCC3**, the -CH₃ groups were disordered over the six cage vertices and a C-C bond distance restraint was used during refinement (DFIX in SHELX). In addition, the -CH₃ group C-atom was refined with an ISOR restraint.

1ET-5FT-RCC3: In the crystal structure, the one -CH₃ group was disordered over 12 possible positions. Due to this disorder, this group was refined with 1,2 and 1,3 bond distance restraints, DFIX and DANG in SHELX, respectively.

1PT-5FT-RCC3: In the crystal structure, the one ethyl tie was severely disordered and it was not possible to accurately locate the methyl group. This is likely due to the flexibility of this group in the crystal structure. Therefore, due to this disorder, the methyl group was not refined as part of the asymmetric unit and neither were the H-atoms for the -CH₂ and -CH₃ groups. However, these atoms were included in the unit cell atom count. It was also necessary to refine the disordered -CH₂- group with 1,2 and 1,3 bond distance restraints, DFIX and DANG in SHELX, respectively.

6ET-RCC3: In the crystal structure, the -CH₃ groups are directed towards the cage windows, but they are disordered over two possible positions. Due to this disorder, this group was refined with a RIGU rigid bond restraint during refinement.

Table S5. Single crystal refinement details for the crystal structures, **1AT-5FT-RCC3·(H₂O)**, **1AT-5FT-RCC3**, and **1AT-5FT-RCC3·(H₂O)**.

	1AT-5FT-RCC3·(H₂O)^[a]	1AT-5FT-RCC3^[b]	1AT-5FT-RCC3·(H₂O)
Wavelength [Å]	Cu-Kα	Cu-Kα	0.7749
Collection Temperature	100 K	400 K	100 K
Formula	C ₈₀ H ₁₁₂ N ₁₂ , H ₂ O	C ₈₀ H ₁₁₂ N ₁₂	C ₈₀ H ₁₁₂ N ₁₂ , H ₂ O
<i>M_r</i>	1259.83	1241.81	1259.83
Crystal Size (mm)	0.27 x 0.26 x 0.16	0.27 x 0.26 x 0.16	0.09 x 0.09 x 0.05
Crystal System	Cubic	Cubic	Cubic
Space Group	F4 ₁ 32	F4 ₁ 32	F4 ₁ 32
<i>a</i> [Å]	25.327(2)	25.490(2)	25.3176(9)
<i>V</i> [Å ³]	16246(5)	16536(4)	16228(2)
<i>Z</i>	8	8	8
D _{calcd} [g cm ⁻³]	1.030	0.996	1.031
μ [mm ⁻¹]	0.475	0.451	0.074
F(000)	5488	5408	5488
2θ range [°]	6.04 – 148.53	6.00 – 117.60	4.96 – 75.82
Reflections collected	15335	14582	47651
Independent reflections,	1395, 0.0279	1002, 0.0249	2853, 0.0414
<i>R</i> _{int}			
Obs. Data [<i>I</i> > 2σ]	1343	926	2628
Data / restraints / parameters	1395 / 9 / 83	1002 / 9 / 78	2853 / 7 / 87
Final R1 values (<i>I</i> > 2σ(<i>I</i>))	0.0484	0.0369	0.0489
Final R1 values (all data)	0.0494	0.0393	0.0540
Final wR(<i>F</i> ²) values (all data)	0.1349	0.1154	0.1440
Goodness-of-fit on <i>F</i> ²	1.110	1.127	1.020
Largest difference peak and hole [e.Å ⁻³]	0.504 / -0.156	0.187 / -0.067	0.383 / -0.189
CCDC	1910114	1910116	1910119

[a] Recorded after reacting a single of **1AT-RCC3** with gaseous formaldehyde. After the reaction, the single crystal was evacuated under dynamic vacuum to remove residual formaldehyde from the crystal pores. The crystal was stored in air prior to the data collection being recorded. [b] Recorded after heating the single crystal from 100 K to 400 K at 50 K/hr, followed by equilibration at 400 K.

Table S6. Single crystal refinement details for the crystal structures, **5FT-RCC3·(H₂O)**, and **1ET-5FT-RCC3·(H₂O)**.

	5FT-RCC3·(H₂O)	1ET-5FT-RCC3·(H₂O)
Wavelength [Å]	0.7749	0.7749
Collection Temperature	100 K	100 K
Formula	C ₇₇ H ₁₀₈ N ₁₂ , 4.63(H ₂ O)	C ₇₉ H ₁₁₀ N ₁₂ , H ₂ O
<i>M_r</i>	1285.21	1245.80
Crystal Size (mm)	0.05 x 0.03 x 0.02	0.06 x 0.05 x 0.01
Crystal System	Cubic	Cubic
Space Group	<i>F</i> 432	<i>F</i> 432
<i>a</i> [Å]	25.2610(8)	25.2521(13)
<i>V</i> [Å ³]	16120(2)	16102(2)
<i>Z</i>	8	8
D _{calcd} [g cm ⁻³]	1.059	1.028
μ [mm ⁻¹]	0.079	0.073
F(000)	5603	5424
2θ range [°]	4.97 – 50.97	4.97 – 57.92
Reflections collected	29858	26818
Independent reflections,	982, 0.0744	1393, 0.0513
<i>R</i> _{int}		
Obs. Data [<i>I</i> > 2σ]	843	1209
Data / restraints / parameters	982 / 0 / 83	1393 / 7 / 86
Final R1 values (<i>I</i> > 2σ(<i>I</i>))	0.0580	0.0471
Final R1 values (all data)	0.0692	0.0564
Final wR(<i>F</i> ²) values (all data)	0.1605	0.1340
Goodness-of-fit on <i>F</i> ²	1.147	1.056
Largest difference peak and hole [e.Å ⁻³]	0.300 / -0.153	0.389 / -0.174
CCDC	1910120	1910117

Table S7. Single crystal refinement details for the crystal structures, **1PT-5FT-RCC3·(H₂O)**, **6ET-RCC3**, and **Cocryst1 (CC3-S, 6ET-RCC3-R)**.

	1PT-5FT-RCC3·(H₂O)	6ET-RCC3	(CC3-S, 6ET-RCC3-R)
Wavelength [Å]	0.7749	Mo-Kα	0.6889
Collection Temperature	100 K	100 K	100 K
Formula	C ₈₀ H ₁₁₂ N ₁₂ , H ₂ O	C ₈₄ H ₁₂₀ N ₁₂	C ₈₄ H ₁₂₀ N ₁₂ , C ₇₂ H ₈₄ N ₁₂
<i>M_r</i>	1259.83	1297.91	2415.42
Crystal Size (mm)	0.04 x 0.03 x 0.01	0.09 x 0.08 x 0.03	0.07 x 0.06 x 0.05
Crystal System	Cubic	Cubic	Cubic
Space Group	<i>F</i> 4 ₃ 2	<i>F</i> 4 ₃ 2	<i>F</i> 4 ₃ 2
<i>a</i> [Å]	25.2201(9)	25.216(4)	24.7202
<i>V</i> [Å ³]	16041.3(17)	16034(8)	15106.2(15)
<i>Z</i>	8	8	4
D _{calcd} [g cm ⁻³]	1.043	1.075	1.062
μ [mm ⁻¹]	0.074	0.064	0.060
F(000)	5488	5664	5232
2θ range [°]	4.98 – 50.96	2.80 – 52.70	4.52 – 51.70
Reflections collected	29631	11436	53093
Independent reflections,	976, 0.0571	1383, 0.0777	1355, 0.0555
<i>R</i> _{int}			
Obs. Data [<i>I</i> > 2σ]	855	1155	820
Data / restraints / parameters	976 / 7 / 86	1383 / 9 / 79	1355 / 115 / 141
Final R1 values (<i>I</i> > 2σ(<i>I</i>))	0.0474	0.0578	0.1181
Final R1 values (all data)	0.0571	0.0680	0.1423
Final wR(<i>F</i> ²) values (all data)	0.1263	0.1609	0.3281
Goodness-of-fit on <i>F</i> ²	1.122	1.062	2.255
Largest difference peak and hole [e.Å ⁻³]	0.391 / -0.164	0.226 / -0.226	0.349 / -0.345
CCDC	1910115	1910113	1910118

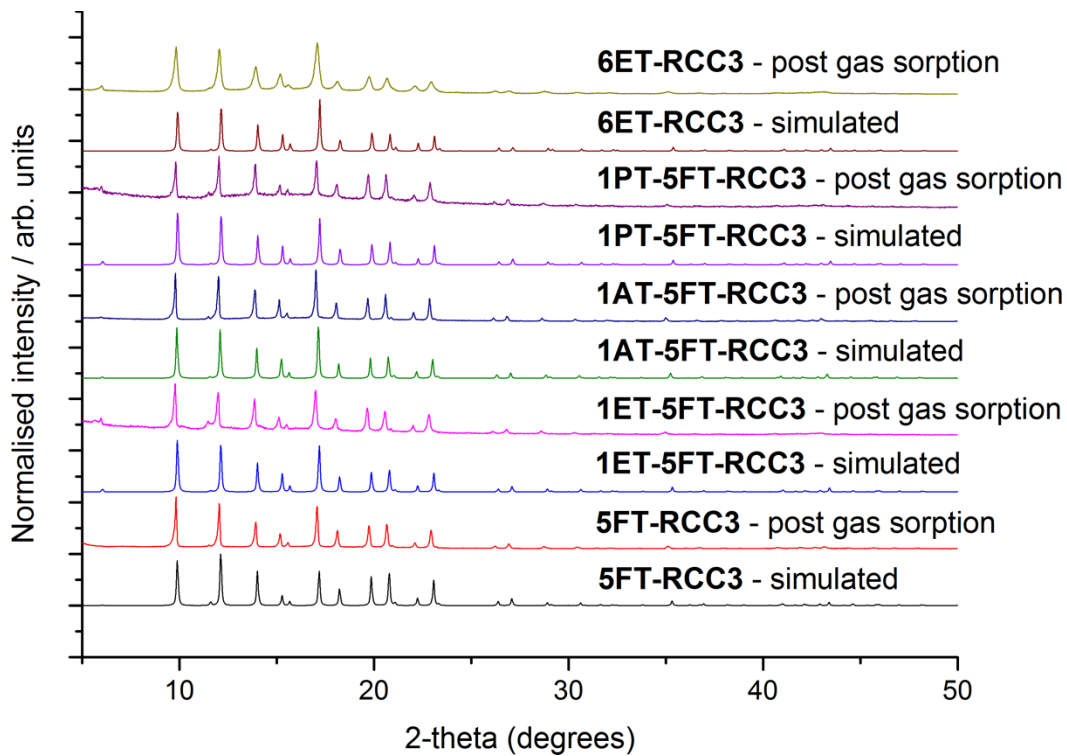


Fig. S16. Post gas sorption PXRD data for the cage series, shown above the simulated PXRD patterns derived from the single crystal structures of each cage. No significant structural change occurs during gas adsorption.

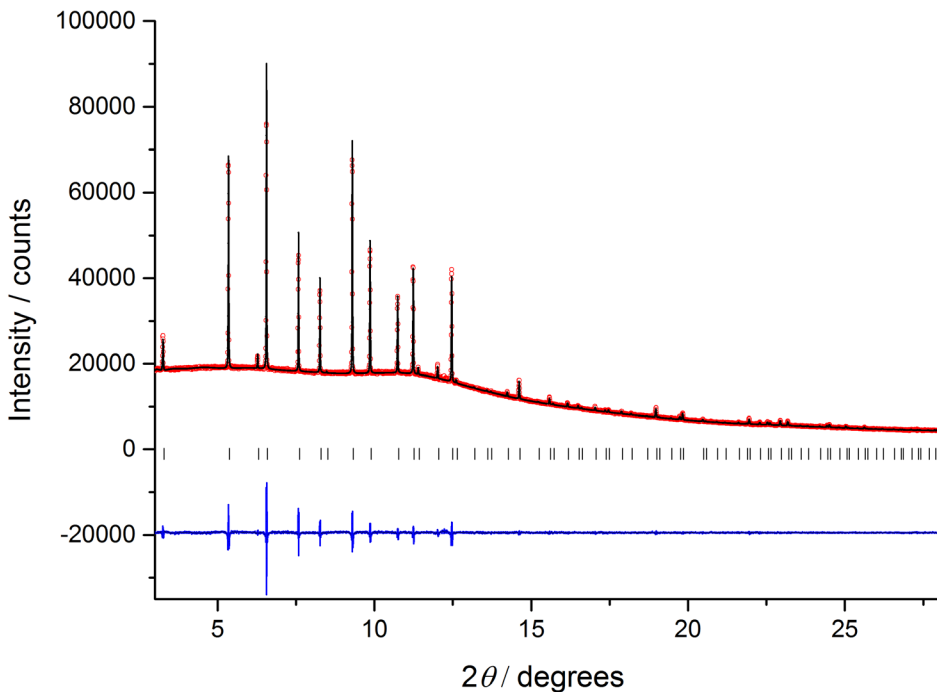


Fig. S17. Le Bail fit for **Cocryst1** crystallised from $\text{CH}_2\text{Cl}_2/\text{acetone}$ and activated under dynamic vacuum. X-ray diffraction was recorded under dynamic vacuum using a sample loaded in an environmental gas cell that was rocked to improve powder averaging. The unit cell choice was based on the refined single crystal data. Final observed (red), calculated (black) and difference (blue) PXRD profiles for Le Bail refinement ($\lambda = 0.825015 \text{ \AA}$, $R_{wp} = 2.234\%$, $R_p = 1.128\%$, $\chi^2 = 2.463$, $a = 24.8586(3) \text{ \AA}$, $V = 15361.4(6) \text{ \AA}^3$, $T = 298 \text{ K}$, $F4_132$).

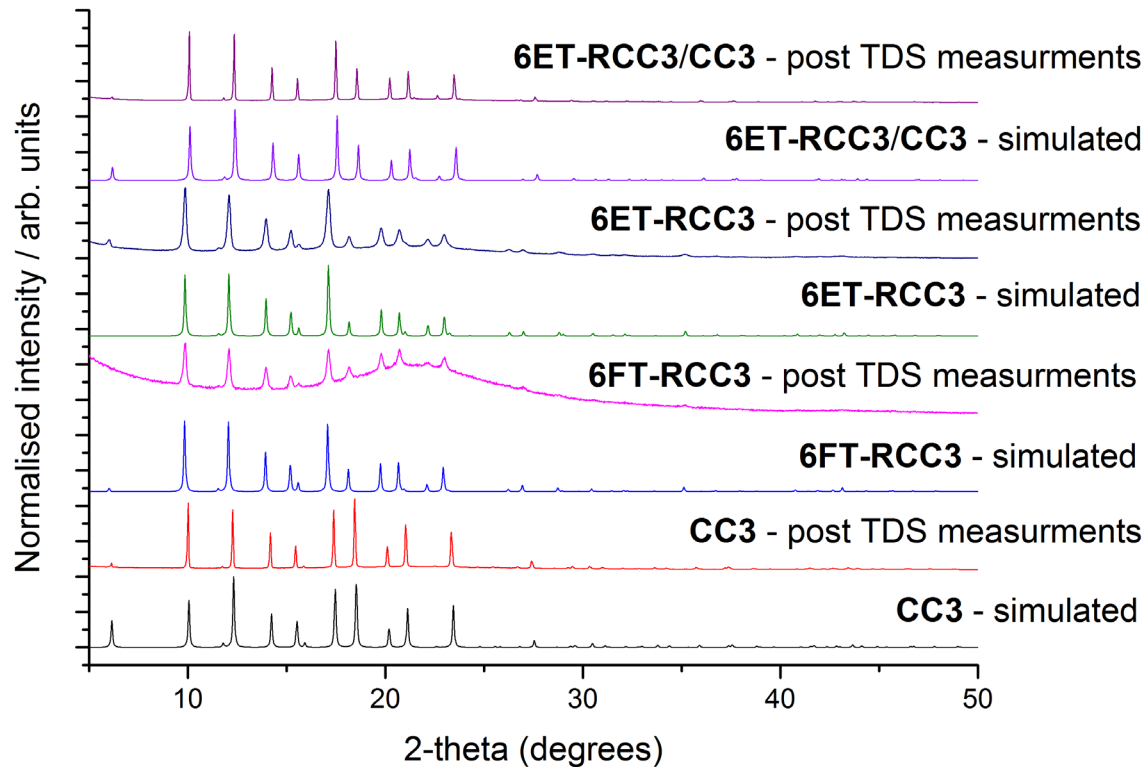


Fig. S18. PXRD data recorded after TDS measurements for **CC3**, **6FT-RCC3**, **6ET-RCC3**, and **Cocryst1** (**CC3-S**, **6ET-RCC3-R**), shown above the simulated PXRD patterns for these structures. We observed a slight loss in crystallinity for the **6FT-RCC3** and **6ET-RCC3** cage materials during these measurements, but the **Cocryst1** (**CC3-S**, **6ET-RCC3-R**) sample remained highly crystalline, see Fig. S19 for Le Bail fit.

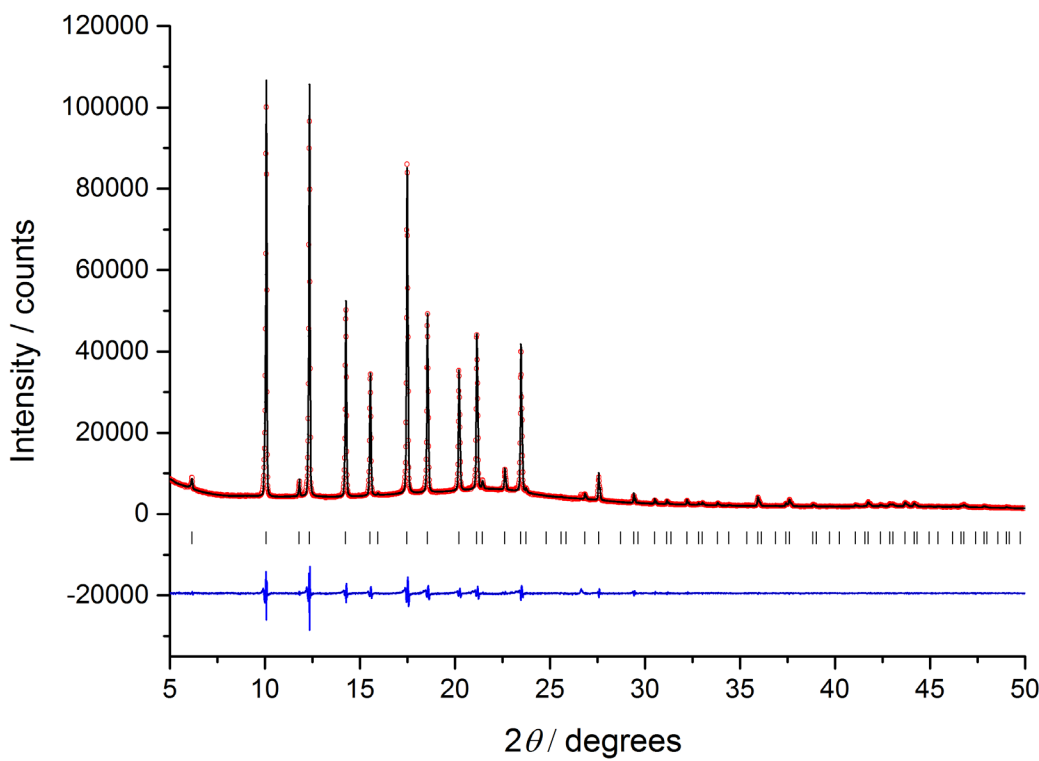


Fig. S19. Le Bail fit for **Cocryst1** (**CC3-S, 6ET-RCC3-R**) crystallised from $\text{CH}_2\text{Cl}_2/\text{acetone}$, activated under dynamic vacuum, and used for TDS measurements. X-ray diffraction was recorded after removal of any adsorbed water from the crystal pores. The capillary was spun during the collection to improve powder averaging and the unit cell choice was based of refined single crystal data. Final observed (red), calculated (black) and difference (blue) PXRD profiles for Le Bail refinement ($R_{wp} = 3.857\%$, $R_p = 2.690\%$, $\chi^2 = 2.667$, $a = 24.846(2)$ Å, $V = 15338(2)$ Å 3 , $T = 298$ K, $F4_132$).

2.9 Additional gas adsorption/desorption isotherms for the isostructural cages

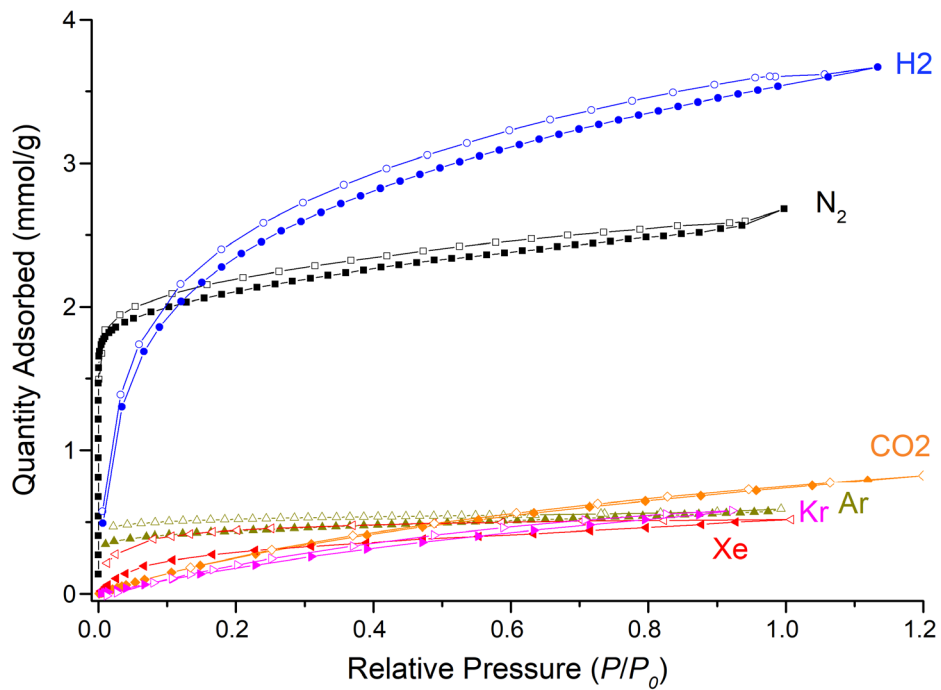


Fig. S20. N_2 (black squares), H_2 (blue circle) and Ar (dark yellow up triangles) at 77 K, CO_2 (orange diamonds) at 298 K, Xe (red left triangles) and Kr (magenta right triangles) at 273 K for **1AT-5FT-RCC3**. Filled and open symbols represent adsorption and desorption isotherms, respectively.

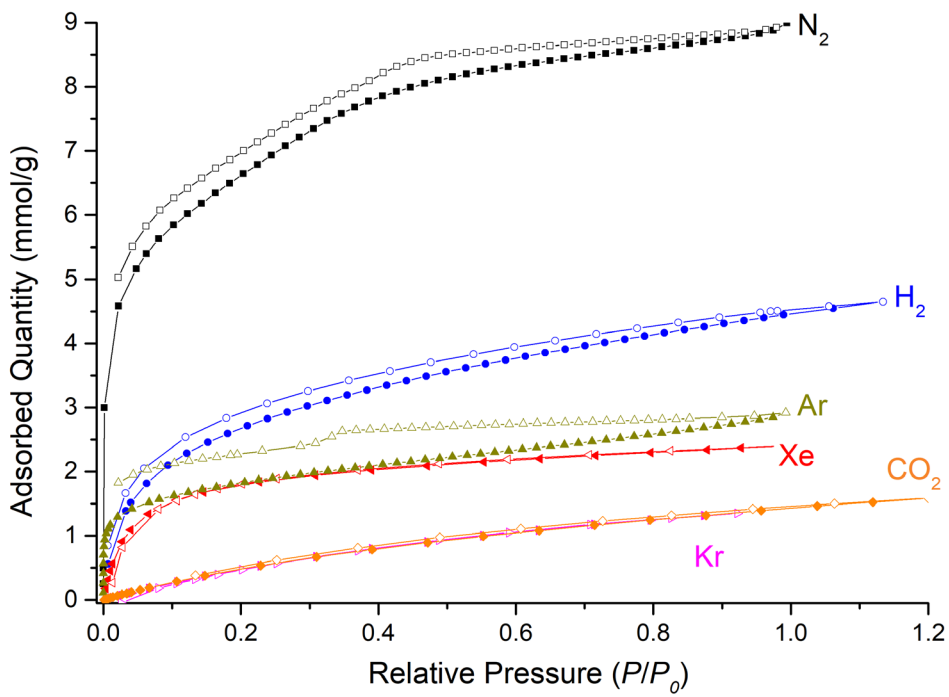


Fig. S21. N_2 (black squares), H_2 (blue circle) and Ar (dark yellow up triangles) at 77 K, CO_2 (orange diamonds) at 298 K, Xe (red left triangles) and Kr (magenta right triangles) at 273 K for **5FT-RCC3**. Filled and open symbols represent adsorption and desorption isotherms, respectively.

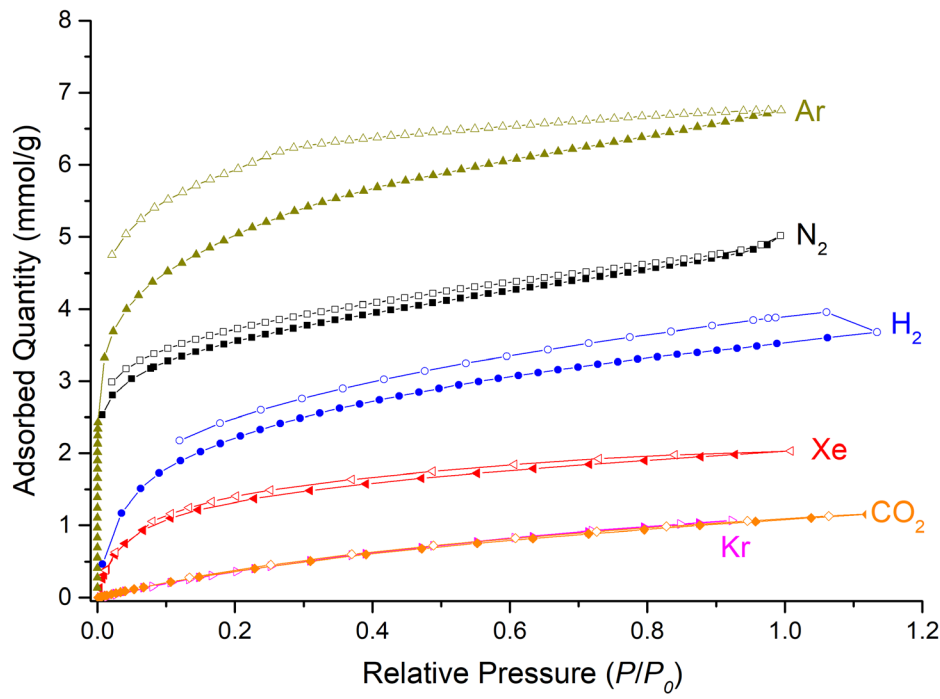


Fig. S22. N_2 (black squares), H_2 (blue circle) and Ar (dark yellow up triangles) at 77 K, CO_2 (orange diamonds) at 298 K, Xe (red left triangles) and Kr (magenta right triangles) at 273 K for **1ET-5FT-RCC3**. Filled and open symbols represent adsorption and desorption isotherms, respectively.

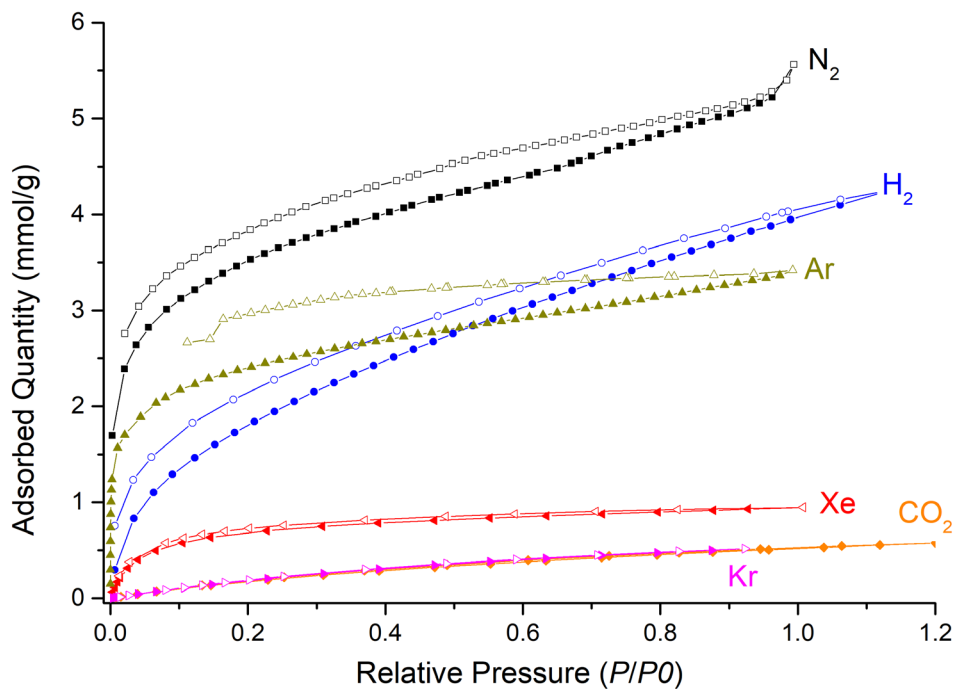


Fig. S23. N_2 (black squares), H_2 (blue circle) and Ar (dark yellow up triangles) at 77 K, CO_2 (orange diamonds) at 298 K, Xe (red left triangles) and Kr (magenta right triangles) at 273 K for **1PT-5FT-RCC3**. Filled and open symbols represent adsorption and desorption isotherms, respectively.

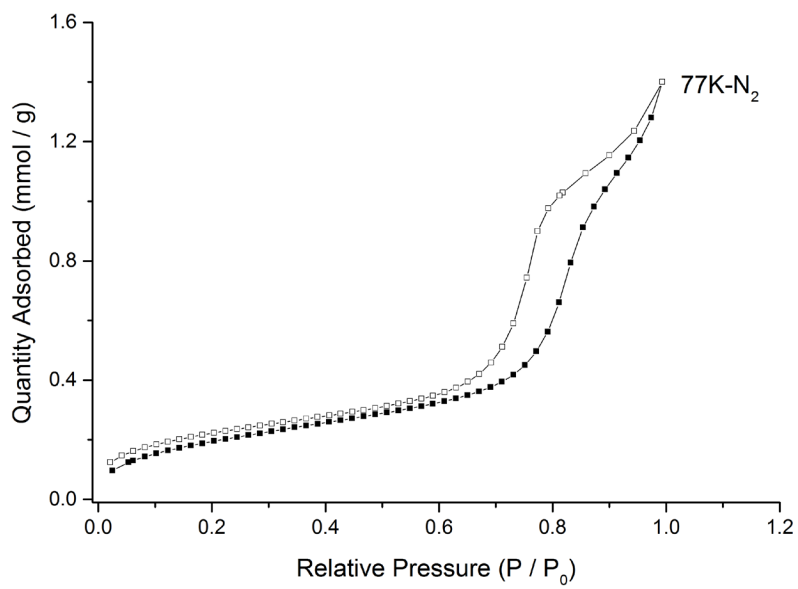


Fig. S24. N₂ isotherm at 77K for **6ET-RCC3**. Filled and open symbols represent adsorption and desorption isotherms, respectively.

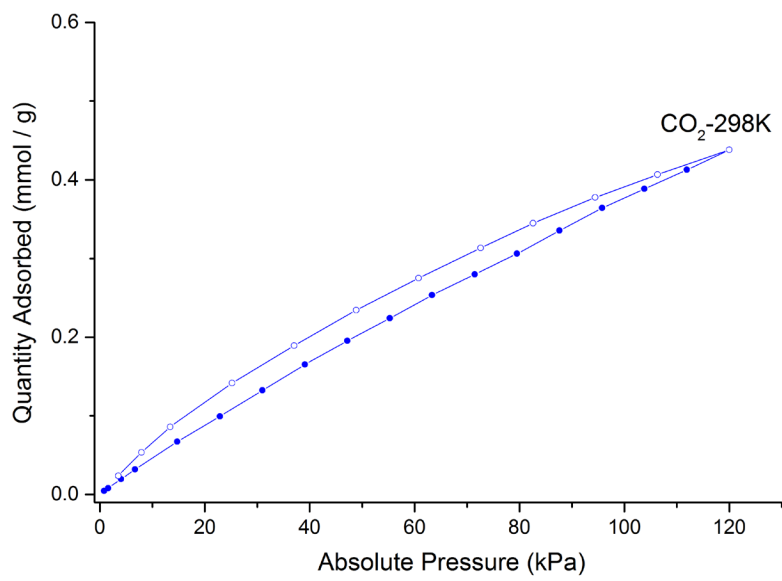


Fig. S25. CO₂ isotherm at 298K for **6ET-RCC3**. Filled and open symbols represent adsorption and desorption isotherms, respectively.

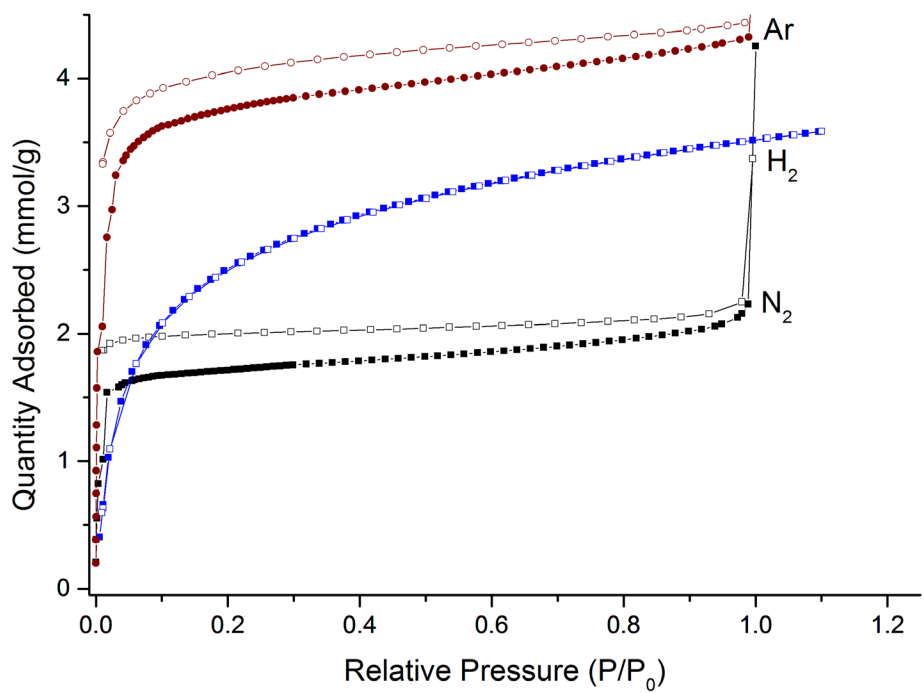


Fig. S26. H_2 (77 K), N_2 (77 K) and Ar (87 K) isotherms of **Cocryst1**. Filled and open symbols represent adsorption and desorption isotherms, respectively.

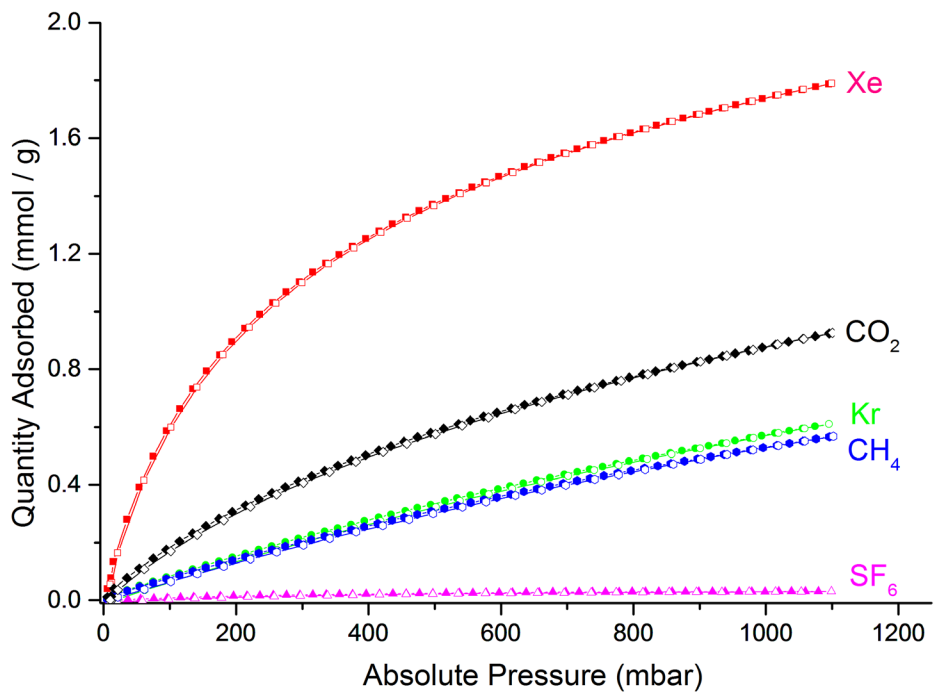


Fig. S27. Isotherms of Xe (red squares), Kr (green circles), CO₂ (black diamonds), CH₄ (blue circles) and SF₆ (magenta up triangles) at 298 K for **Cocryst1**. Filled and open symbols represent adsorption and desorption isotherms, respectively.

2.10 Computational methods (classical simulations)

2.10.1 Pore-limiting envelope

Molecular dynamics (MD) simulations were used to calculate a time-averaged, pore-limiting envelope (PLE) for the isostructural series of post-synthetically modified cages in this study. Individual frames of these MD simulations were extracted; with the pore-limiting diameter (PLD) determined for each of them using the high-throughput geometry-based analysis tool Zeo++ (70). Histograms of these values form the respective PLEs for the systems studied here and are displayed in Fig 1C. PLEs account for the flexibility, intramolecular vibrations and molecular motion about the equilibrium crystal structure. For MD simulations, the experimental single-crystal structures were used as the starting configuration. The MD simulations were carried out using DL_POLY_2.20 (71), with a $2 \times 2 \times 2$ supercell. All cage crystals were modelled using the OPLS force field with a cutoff distance of 10 Å. An NPT ensemble at 1 atm and 298 K was used with the Hoover barostat and thermostat, and both had a time constant of 0.5 ps. A timestep of 0.5 fs was used, with the system first equilibrated for 100 ps, followed by a production run of 2 ns, with a frame output every 1 ps. This MD trajectory was used to generate a PLE for the system.

2.10.2 Adsorption and diffusion simulations

To account for quantum diffraction effects in classical molecular simulations, the so-called Feynman–Hibbs (FH) effective potentials may be used (44). The quadratic FH potential, $U_{\text{FH}}(r)$, operates on a given classical model potential, $U_{\text{C}}(r)$, and is given by

$$U_{\text{FH}}(r_{ij}) = U_{\text{C}}(r_{ij}) + \frac{\hbar^2}{24\mu_{ij}k_B T} \left[U_{\text{C}}''(r_{ij}) + 2 \frac{U_{\text{C}}'(r_{ij})}{r_{ij}} \right]$$

where r_{ij} is the separation distance between particles i and j , \hbar the reduced Planck constant, k_B the Boltzmann constant, T the temperature, and μ_{ij} the reduced mass, which equates to $m_i m_j / (m_i + m_j)$ with m_i and m_j being the masses of the particles. In our simulations of hydrogen adsorption/diffusion at a temperature of 77 K or below, $U_{\text{C}}(r)$ took the form of Lennard–Jones (LJ) potential. Together with a simple charge-charge Coulomb potential, the total (non-bonded) interaction energy is given by

$$U^{\text{tot}}(r_{ij}) = 4\epsilon_{ij} \left[\left(\frac{\sigma_{ij}}{r_{ij}} \right)^{12} - \left(\frac{\sigma_{ij}}{r_{ij}} \right)^6 \right] + \frac{4\epsilon_{ij}}{r_{ij}^2} \frac{\hbar^2}{24\mu_{ij}k_B T} \left[132 \left(\frac{\sigma_{ij}}{r_{ij}} \right)^{12} - 30 \left(\frac{\sigma_{ij}}{r_{ij}} \right)^6 \right] + \frac{q_i q_j}{4\pi\epsilon_0 r_{ij}}$$

where ϵ_{ij} and σ_{ij} are the LJ potential well depth and hard-core diameter, respectively, q_i and q_j the partial atomic charges, and ϵ_0 the vacuum permittivity.

The model proposed by Levesque *et al.* (72) was used to describe hydrogen as a rigid two-site molecule with the H–H bond length fixed at 0.74 Å; partial atomic charges were placed on the two hydrogen atoms and the centre of mass of the hydrogen molecule to reproduce the quadrupole moment of molecular hydrogen in gas phase. Despite the same force-field parameters (of Levesque *et al.*) being used for both H₂ and D₂, their interactions with the surroundings may

still be different because of the use of the FH effective potentials. A real-space cutoff of 12.0 Å was applied to all LJ interactions, while long-range Coulomb interactions were handled by the Ewald summation technique with a relative precision of 10^{-6} . The Lorentz–Berthelot combining rules were used to calculate the LJ cross-parameters for host–guest and guest–guest interactions. For all the porous organic cage crystals simulated, one unit-cell of the experimental crystal structure was used, with periodic boundary conditions exerted in three dimensions. In the cases of flexible-host simulations, the experimental crystal structures were used as starting configurations. The OPLS force field (73) was used to assign force-field parameters (for both bonded and non-bonded interactions) and partial atomic charges to all the cage molecules.

The molecular simulation software for adsorption and diffusion in flexible nanoporous materials, RASPA 2.0 (74), was used throughout this study. Gas adsorption simulations were carried out using a hybrid grand-canonical Monte Carlo (GCMC) / molecular dynamics (MD) scheme, which allows for direct sampling of host motions in adsorption simulations. The hybrid MC/MD moves consisted of an MD path computed in the isoenthalpic–isobaric (*NPH*) ensemble. Each MD move was performed for 5 timesteps of 0.5 fs each, with a probability of 2% in the simulation. The MD runs allowed the molecular cage crystals to relax upon the loading of the guest molecules, with newly relaxed configurations either accepted or rejected by the MC sampling rule. Other trial MC moves included insertion, deletion, translation, rotation, reinsertion and identity swap (in the case of a gas mixture); these moves were randomly attempted with equal probabilities. All the GCMC/MD and GCMC simulations involved an 800,000-cycle equilibration period followed by a 200,000-cycle production run; one cycle consisted of n MC moves, with n being equal to the number of adsorbate molecules (or 20, whichever is greater). In a typical GCMC/MD simulation performed here, the sampled MD path amounted to approximately 1 ns in total.

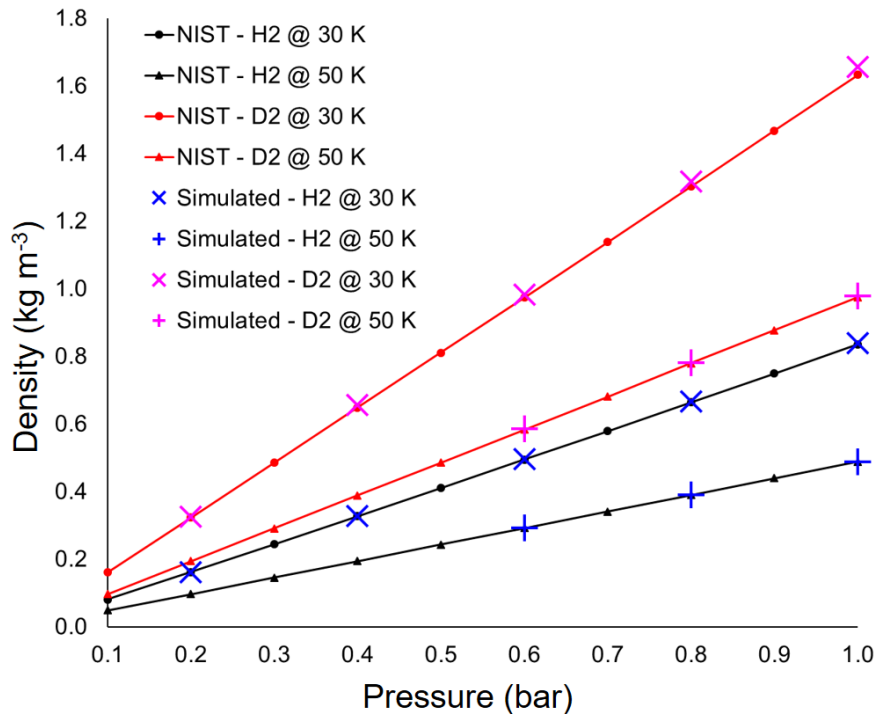


Fig. S28. Comparison of simulated and experimental bulk gas densities of H₂ and D₂ at 30 K and 50 K for a range of pressures from 0.1 bar to 1.0 bar. Monte Carlo simulations in the isothermal–isobaric (*NPT*) ensemble were performed to predict the gas densities, in conjunction with the Feynman–Hibbs quantum effective potentials. The experimental densities were retrieved from the NIST Standard Reference Database Number 85 (DOI: <https://doi.org/10.18434/T4D303>).

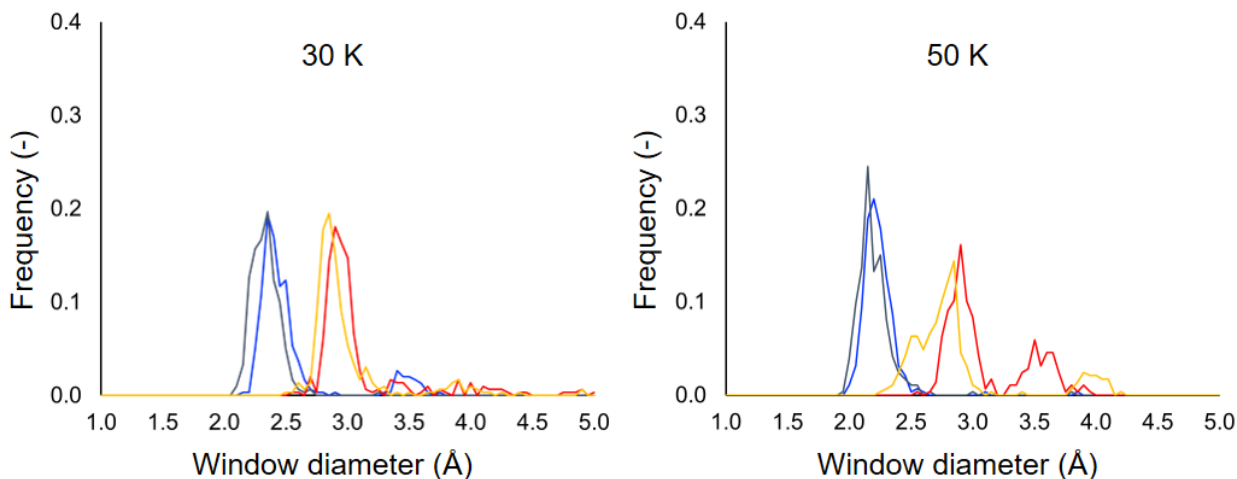


Fig. S29. Time-averaged, window-size envelopes for all four windows of the same cage molecule obtained from a 300-ps MD trajectory, sampled every 1 ps, at 30 K or 50 K at 1 bar. Among the four cage windows, two have two methyl groups at the window (colored in grey and blue, respectively) and the other two have one methyl group at the window (colored in red and yellow, respectively). *NPT* MD simulations were performed on the periodic structure of the cocrystal, which were first equilibrated for 2 ns before statistics were collected.

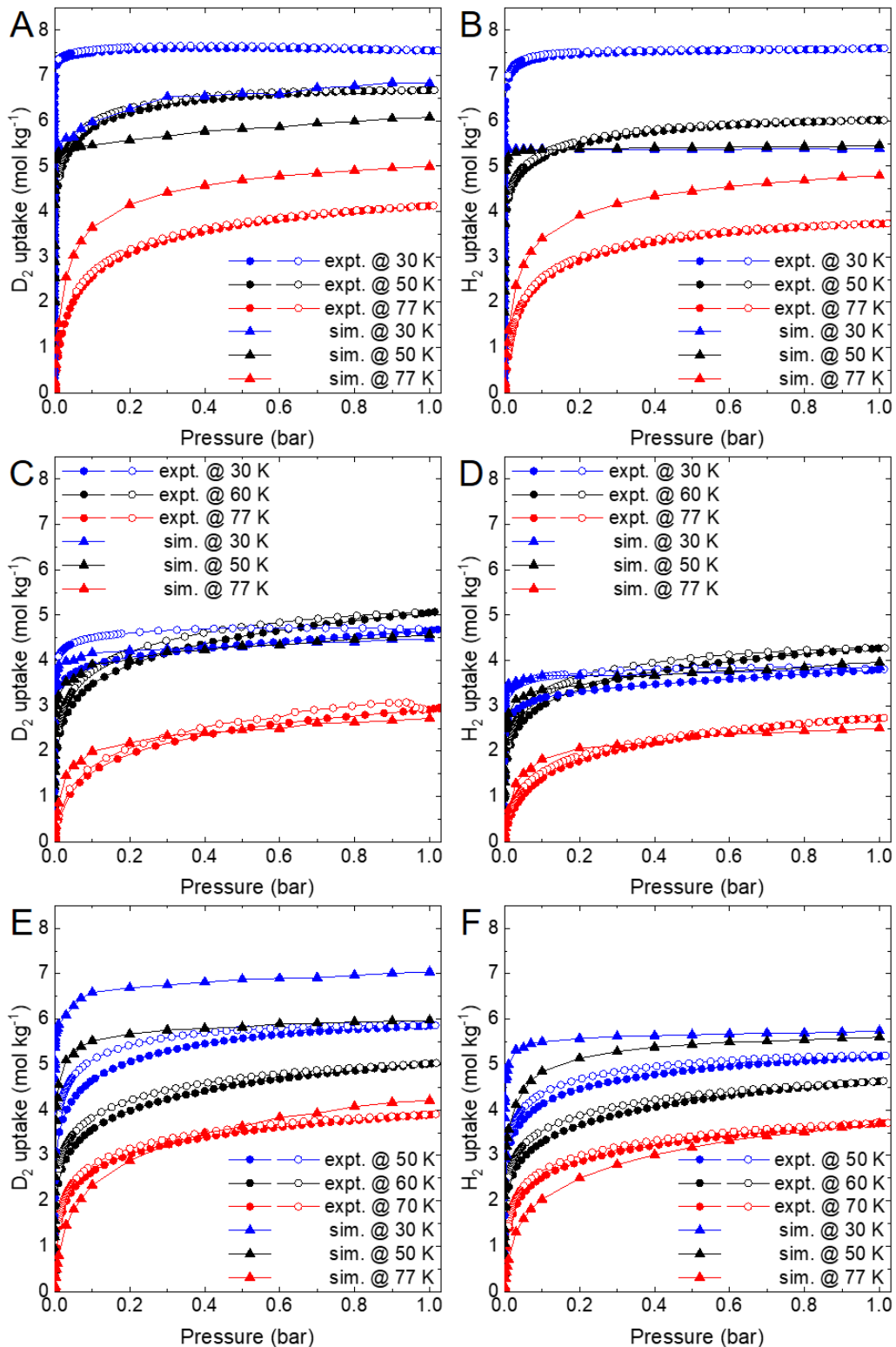


Fig. S30. Comparison of simulated and experimental isotherms of D₂ (A, C, E) and H₂ (B, D, F) for CC3 (A, B), 6ET-RCC3 (C, D) and Cocryst1 (E, F).

2.10.3 Free energy profiles of gas diffusion in cage crystals

Molecular diffusion in nanometer confinements, such as those present in the crystal structures simulated here, can be so slow that the timescale for a particle to hop from one free-energy minimum to the next becomes too large to be reached by routine application of molecular dynamics simulations. For example, a guest molecule may be trapped inside a cage molecule, and the actual time needed for it to escape through a cage window is negligible compared to the time it spends inside the cage. Such a process can be considered an activated process, which may be alternatively probed by rare-event simulation methods such as transition state theory (TST). A comprehensive demonstration of the method in studying transport of adsorbates in nanoporous adsorbents was given by Dubbeldam *et al* (75).

Free energy profiles (Figure 5 D–F, main text) were calculated using Monte Carlo simulations in the canonical (*NVT*) ensemble, together with the Widom particle insertion method. During the simulation, a probe molecule (*i.e.*, H₂ or D₂) was inserted at many random positions in the cage crystal structure to measure the energy required for or obtained by each of the insertions of the molecule into the system. This energy is mapped onto the reaction coordinate q to produce a free-energy profile, using

$$\beta F(q) = -\ln\langle e^{-\beta \Delta U} \rangle_N$$

where $\beta = 1/(k_B T)$ with k_B being the Boltzmann constant and T being the temperature, and $\langle e^{-\beta \Delta U} \rangle_N$ is the average Boltzmann factor of all N sampled positions in the plane perpendicular to the reaction coordinate q .

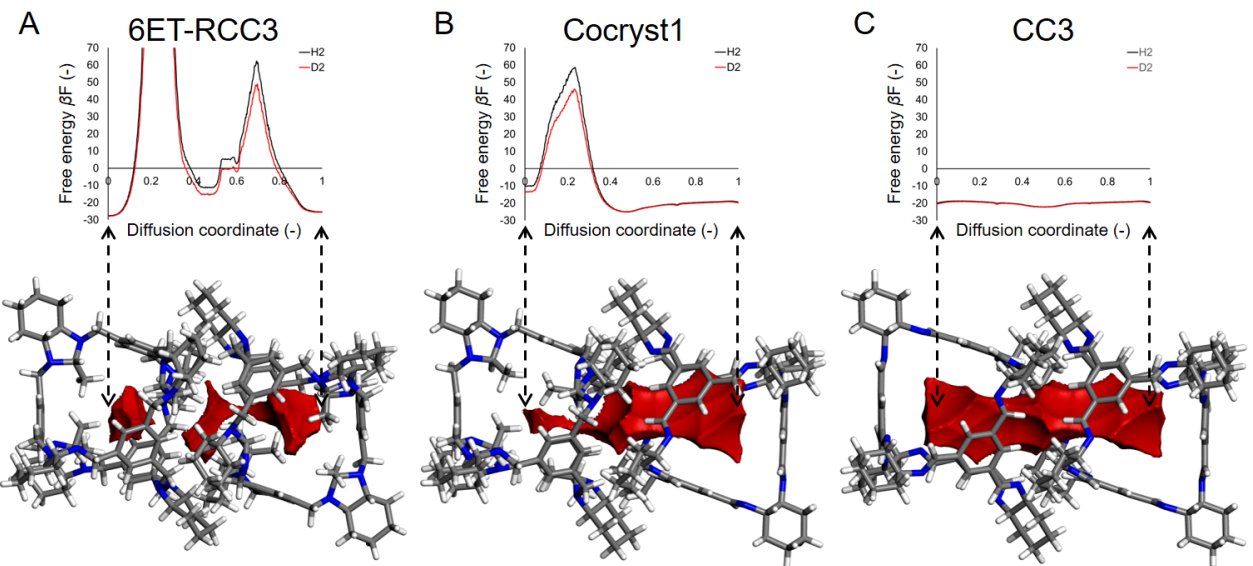


Fig. S31. Free energy profiles were calculated for the diffusion pathways using the respective crystal structures; only the relevant two cage molecules involved are shown here. The diffusion pathway in (A) runs through a **6ET-RCC3** cage window with two methyl groups (left cage) and a second **6ET-RCC3** cage window with one methyl group (right cage); the diffusion pathway in (B) runs through a **6ET-RCC3** cage window with one methyl group (left cage) and a neighboring **CC3** cage window (right cage). Gray, white and blue atoms represent carbon, hydrogen and nitrogen, respectively; pore spaces inside the cage molecules, defined by a spherical probe with diameter 2.2 Å, are colored in red.

2.11 Host–guest binding energies

Path integral molecular dynamics (PIMD) simulations were combined with quantum mechanical interaction evaluations to further probe the diffusion behaviors of H₂ and D₂ in the cage molecules, explicitly accounting for the quantum mechanical nature of both the electrons and nuclei. Since path integral simulations are typically two orders of magnitude more expensive to perform than when treating the nuclei classically, we focused only on an isolated **6ET-RCC3** cage molecule with one gas molecule (*i.e.*, H₂ or D₂) diffusing out of the cage. Further computational cost savings were made by using the self-consistent-charge density-functional tight-binding DFTB3 method (76) for calculation of the interactions from evaluation of the electronic structure, together with a dispersion correction scheme based on UFF (77).

We benchmarked the DFTB3-UFF method for describing the energetics of our host–guest systems (*i.e.*, **6ET-RCC3** with H₂ or D₂) against DFT-D3 methods with the BLYP and PBE density functionals. The 3OB parameterization was used for all DFTB3 calculations (78). For DFT based calculations, the MOLOPT-DZVP basis set was used for all elements, together with the Goedecker–Teter–Hutter pseudopotentials (79, 80). The auxiliary planewave basis set was defined by an energy cutoff of 500 Ry, accompanied by a relative cutoff of 50 Ry for the Gaussian basis set collocation. During each self-consistent-field cycle, the electronic structure was minimized to a tolerance of 10⁻⁸ Hartree. Calculations were performed with the CP2K simulation package (<https://www.cp2k.org/>). The host–guest binding energies were defined as

$$E_{\text{binding}} = E(\text{host} \cdots \text{guest}) - E(\text{host}) - E(\text{guest})$$

where $E(\text{host} \cdots \text{guest})$, $E(\text{host})$, and $E(\text{guest})$ are the total energies of the guest-loaded **6ET-RCC3** host, empty **6ET-RCC3** host, and isolated guest molecule (H₂ or D₂), respectively. Table S6 reports all the binding energies obtained using different methods, which clearly shows that the DFTB3-UFF method is not only computationally efficient but can also describe the systems correctly. Therefore, all the PIMD simulations made use of the DFTB3-UFF method for electronic structure evaluations.

Table S8. Gas-phase host–guest binding energies for a single H₂ or D₂ molecule at the centre of an isolated **6ET-RCC3** cage molecule.

Electronic structure method	Dispersion correction	E_{binding} (kJ mol ⁻¹)
DFTB3	UFF	-13.95
DFTB3	D3	-48.58
BLYP	D3	-14.93
PBE	D3	-17.85

2.12 Minimum-energy pathways for H₂ diffusing through cage windows

We performed climbing-image nudged elastic band (CI-NEB) calculations to determine the minimum-energy pathway (MEP) for a single H₂ molecule migrating through each of the four windows of the **6ET-RCC3** cage molecule. The same DFTB3-UFF setup as described above was used for all CI-NEB calculations.

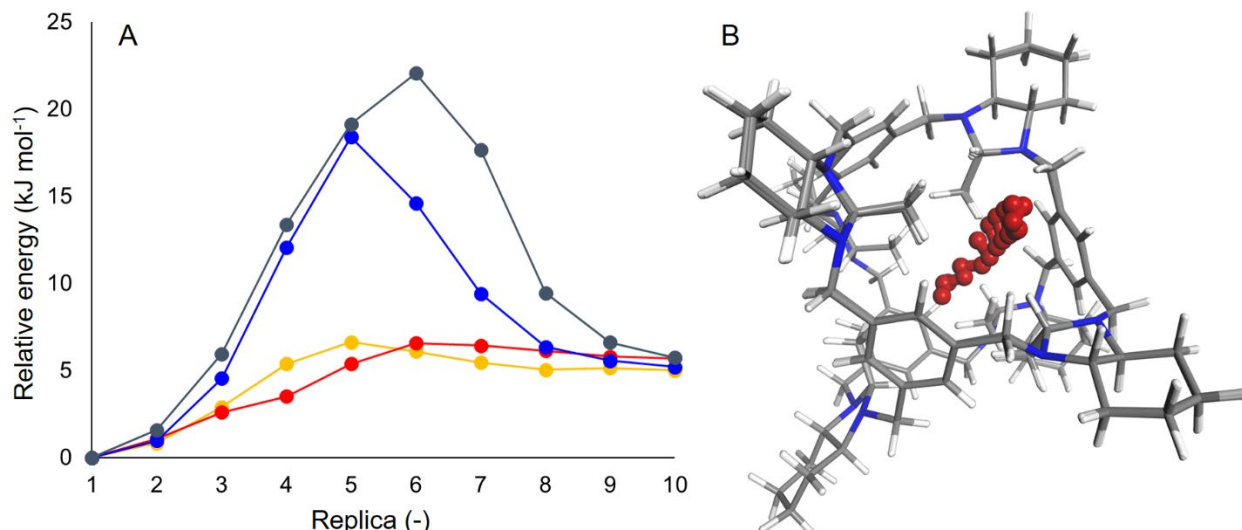


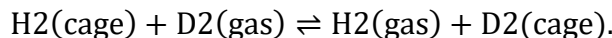
Fig. S32. (A) Minimum-energy pathways (MEPs) for H₂ migration through the four windows of the **6ET-RCC3** cage molecule, starting from the center of the cage. Among the four cage windows, two have two methyl groups at the window (colored in grey and blue, respectively) and the other two have one methyl group at the window (colored in red and yellow, respectively). (B) An overlay of all ten CI-NEB replicas (*i.e.*, the various molecular configurations) along the MEP colored in yellow in (A). White, grey and blue atoms of the cage molecule represent hydrogen, carbon and nitrogen, respectively; red atoms represent the H₂ molecule.

2.13 Path integral molecular dynamics simulations and free energy calculations

System. As discussed above, direct simulation of the periodic cage crystal structures with PIMD is intractable because of the large system sizes (for example, the cocrystal structure comprises more than 1,500 atoms in the unit cell). Since molecular cage crystals are assembled by packing of discrete cage molecules, many porosity-related properties of the crystal structure closely follow those of the constituent molecular subunits; for example, the pore-limiting diameter in the **CC3** crystal structure is governed by the sizes of cage windows. This allows us to study isolated cage molecules to understand the properties of the cage crystals, which has been shown previously to capture the essential features of the diffusion process of interest (81).

Statistical Mechanics. To account for quantum Boltzmann statistics of the nuclear degrees of freedom, we used imaginary time path integral molecular dynamics (PIMD) (82). This technique is based on an isomorphism between the quantum statistical mechanics of a system and the classical statistical mechanics of a so-called ring polymer made of multiple replicas of the system (83). This method rigorously accounts for the statistics of zero-point fluctuations and quantum tunneling but does not include effects arising from the indistinguishability of identical atoms. This approximation could become problematic for the atoms in the H₂ or D₂ molecule at low temperatures (84). However, including the effects of exchange within PIMD simulations leads to a pathological sign problem (85) and posterior corrections to account for it are non-trivial. We therefore performed all the simulations assuming distinguishable atoms, keeping in mind that the approximation may not be an accurate one.

Relative population of D₂ over H₂ inside the 6ET-RCC3 cage. The relative population of D₂ over H₂ inside the cage at a specific temperature is a measure of the relative preference of D₂ over H₂, which may be compared with the experimental D₂/H₂ selectivity. To calculate relative population, we consider a reversible substitution of a molecule of H₂ inside the cage with a molecule of D₂ in the gas phase:



The equilibrium constant (α) of this substitution gives the relative abundance of D₂ over H₂ inside the cage over the gas phase at the temperature T and can be expressed as (86):

$$-k_B T \ln(\alpha) = \{A[\text{D}_2(\text{cage})] - A[\text{H}_2(\text{cage})]\} - \{A[\text{D}_2(\text{gas})] - A[\text{H}_2(\text{gas})]\}$$

where A denotes the Helmholtz free energy of the system and k_B is the Boltzmann constant. The free energy difference is calculated by performing a thermodynamic integration over the masses (87), evaluating:

$$-k_B T \ln(\alpha) = - \int_{m_{\text{H}_2}}^{m_{\text{D}_2}} dm [T(m; \text{cage}) - T(m; \text{gas})]/m$$

where m_{D_2} and m_{H_2} are the atomic masses of the D₂ and H₂ molecules, respective; $T(m; \text{cage/gas})$ is the expectation value of the quantum kinetic energy of the guest molecule with the atomic mass m in the cage or gas phase. The integral was discretized with three points, selected using the quadrature of Ceriotti and Markland (88). PIMD simulations were used to calculate the

quantum kinetic energies of H₂ and D₂ inside the cage molecule and in the gas phase. The simulations were performed using i-PI (89) in the *NVT* ensemble at temperatures $T = 30$ K, 40 K, 50 K, 77 K and 100 K. Quantum fluctuations were enforced using the PIGLET thermostat (90), with the following parameters:

T (K)	Number of replicas	GLE parameters	Centroid thermostat
30	32	$N_s=8$, $hw/kT = 500$, PIGLET	OPT(H), $N_s=8$ wmax / wmin= 10^4
40	32	$N_s=8$, $hw/kT = 200$, PIGLET	OPT(H), $N_s=8$ wmax / wmin= 10^4
50	32	$N_s=8$, $hw/kT = 200$, PIGLET	OPT(H), $N_s=8$ wmax / wmin= 10^4
77	24	$N_s=8$, $hw/kT = 100$, PIGLET	OPT(H), $N_s=8$ wmax / wmin= 10^4
100	16	$N_s=8$, $hw/kT = 100$, PIGLET	OPT(H), $N_s=8$ wmax / wmin= 10^4

These parameters were retrieved from the online repository, <http://gle4md.org/>. The DFTB+ code (91) was used to perform force evaluations. The equations of motion were integrated using a BAOAB scheme (92) using a time step of 0.5 fs. The simulations were run for 20 ps and the quantum kinetic energy was sampled at each step. The error in the relative population was calculated by propagation of the error from the quantum kinetic energy, which was calculated as the standard error of the time series obtained from the PIMD simulations (Fig. 5 K, Main Text).

Free energy profiles for H₂ and D₂ diffusing through cage windows. Free energy profiles were calculated using a combination of PIMD and umbrella sampling (93). The cage window of **6ET-RCC3** with the lowest energy barrier, as estimated by the CI-NEB calculations (fig. S32), was investigated. The order parameter is defined as:

$$s = (r_{\text{guest}} - r_{\text{cage}}) \cdot (r_{\text{window}} - r_{\text{cage}}) / |(r_{\text{window}} - r_{\text{cage}})|^2$$

where r_{guest} , r_{cage} and r_{window} are the position vectors of the guest molecule, the center of the cage and the center of the window, respectively. $s = 0$, $s = 1$ and $s > 1$ correspond to the guest molecule located at the center of the cage, in the transition state with the guest molecule at the center of the window and outside the cage, respectively. The cage is roughly an irregular octahedron with four windows that are diagonally opposite to phenyl rings. The center of the window of interest is defined as the centroid of the three carbon atoms highlighted in red in fig. S33. The center of the cage molecule is defined as the centroid of the six carbon atoms: three highlighted in red and three in orange (fig. S33).

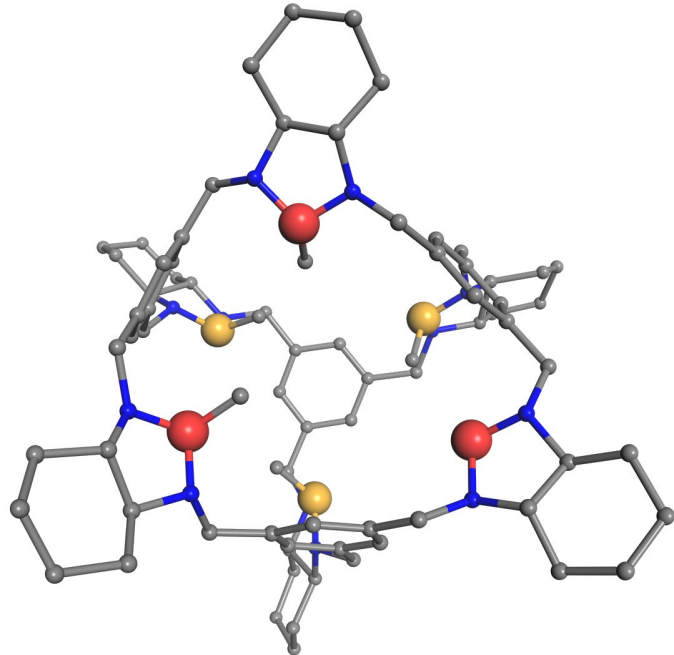


Fig. S33. Definition of the window center and cage center for **6ET-RCC3**. Carbon atoms that bridge the two nitrogen atoms belonging to the same vertex are enlarged and highlighted in red or orange.

A total of 50 harmonic restraints uniformly centered between $s = 0.0$ and $s = 4.5$ were used. Harmonic force constants were set to $K = 150 \text{ kJ mol}^{-1}$ and $K = 500 \text{ kJ mol}^{-1}$ for the first 40 and the remaining 10 restraints, respectively. To prevent the guest molecule from flying away from the cage molecule, a wall was applied at

$$s' = \sqrt{\left| (r_{\text{guest}} - r_{\text{cage}}) \right|^2 - \left[(r_{\text{guest}} - r_{\text{cage}}) \cdot (r_{\text{window}} - r_{\text{cage}}) / \left| (r_{\text{window}} - r_{\text{cage}}) \right| \right]^2} = 0.20.$$

The PIMD simulations were performed at 50 K using i-PI; PLUMED (94) was used to apply the bias on the centroid of the ring polymer Hamiltonian. The computational setting was kept the same as in the previous sections. For each restraint, a simulation was run for 10 ps. A weighted histogram analysis method, as implemented by Grossfield (95), was used to harness unbiased free energy curves. This process was repeated four times using different starting configurations, as well as different random number seeds, to obtain an averaged free energy profile with error bars (Figure 5 L, Main Text).

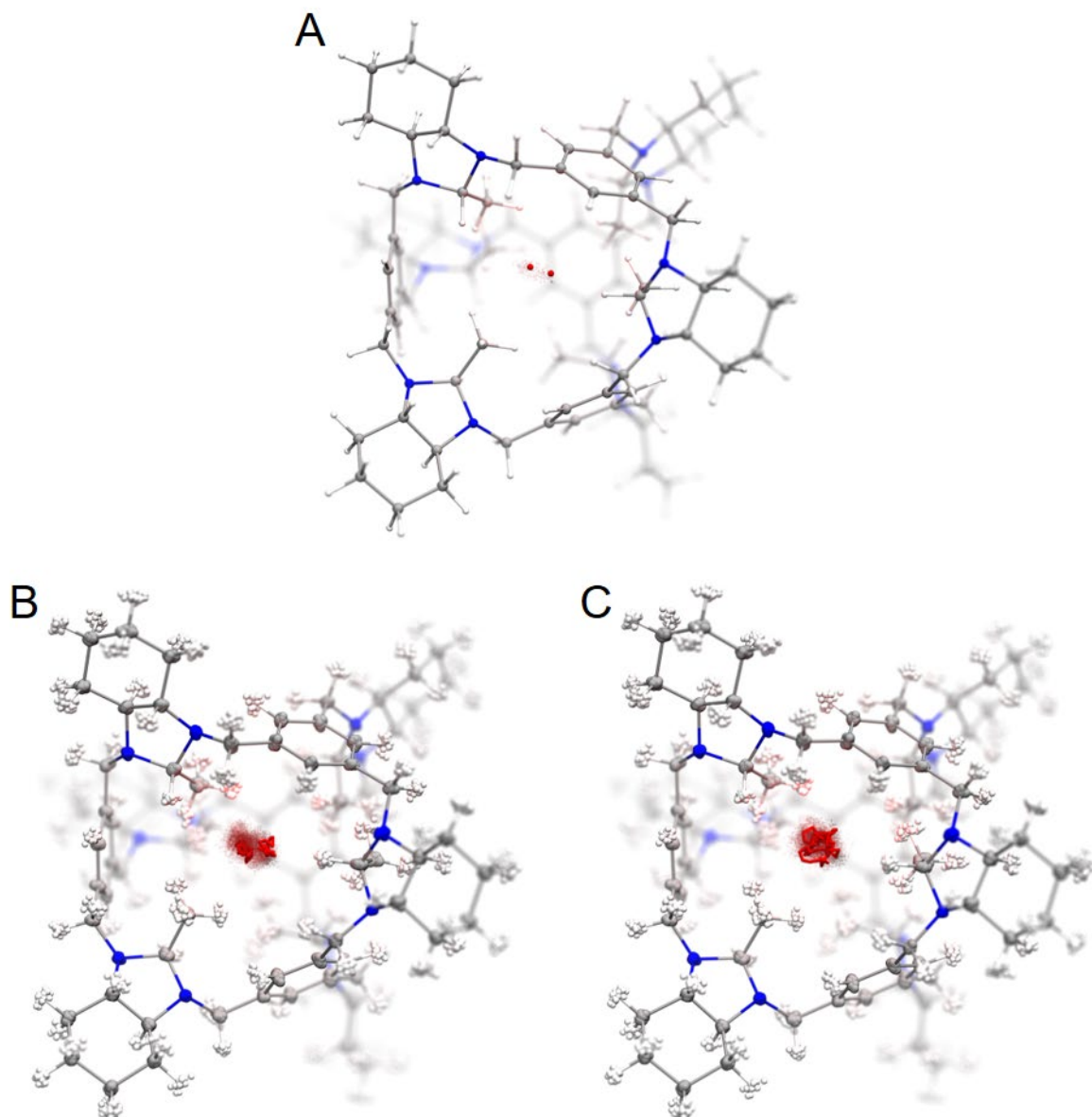


Fig. S34. Transition states for the translocation of (A) a classical H_2 molecule, (B) a quantum D_2 molecule, and (C) a quantum H_2 molecule. A single snapshot (at one timestep) is shown for all three cases; in (B, C), an overlay of all 32 replicas from the PIMD simulation is shown, extracted from the umbrella sampling that is closest to the top of the free-energy barrier. White, grey and blue atoms represent hydrogen, carbon and nitrogen of the **6ET-RCC3** cage molecule. H_2 and D_2 are shown in red; the classical H_2 is represented by two balls (A), while the quantum D_2 (B) and H_2 (C) are in the ‘licorice’ representation, clearly showing the nuclear quantum fluctuations. To give a better visualization of the fluctuations of the translocating molecule (D_2 or H_2), the positions taken from 100 transition-state configurations are shown as translucent dots.

2.14 Synthesis details of the isostructural cages

Synthesis of 1AT-5FT-RCC3. 1AT-RCC3 (200 mg, 0.17 mmol) solid was ground into fine powder and transferred into a 12 mL open glass vial. The open cage-containing vial was then placed into a larger 50 mL glass vessel that contained solid paraformaldehyde (200 mg). The glass vessel was sealed, and then heated at 60 °C in oil bath to generate a gaseous formaldehyde atmosphere. [CAUTION: formaldehyde is a class I human carcinogen and it should only be handled in contained environment by trained personnel with suitable personal protective equipment]. The reaction was left sealed at 60 °C for 12 hours, before the reaction was cooled to room temperature. The solid in the vial was retrieved and dried under dynamic vacuum at 40 °C to remove the surface adsorbed formaldehyde. 1AT-5FT-RCC3 (crude yield = 205 mg, 97.5 %) was obtained as a crystalline white solid. ^1H NMR (CDCl_3 , 400 MHz) δ 7.20–6.95 (m, 12H, -ArH), 4.14–3.86 (m, 12H, -ArCH₂), 3.45–3.00 (m, 12H, -ArCH₂ and 10 H, -NCH₂N-), 2.20–2.40 (m, 12H, CH on cyclohexane), 2.15–1.75 (m, 24H, CH₂ on cyclohexane), 1.40–1.00 (m, 24H, CH₂ on cyclohexane), 0.85–0.40 (m, 6H, CH₃) ppm; ^{13}C NMR (CDCl_3 , 100 MHz): δ 140.1, 123.6, 78.4, 68.8, 57.8, 57.3, 30.9, 29.4, 24.4 ppm. IR (KBr pellet, ν) 2925 (s), 2857 (s), 2795 (w), 1669 (w), 1605 (m), 1446 (s), 1349 (w), 1335 (s), 1313 (w), 1291 (m), 1216 (w), 1185 (m), 1121 (m), 1065 (w), 1039 (w), 1005 (m), 953 (w), 907 (m), 859 (m), 834 (m), 736 (w), 685 (m), cm⁻¹. MS (ES+) 1241.9 ([M+H]⁺). Accurate mass calculated for $[\text{C}_{80}\text{H}_{113}\text{N}_{12}]^+$: 1241.921. Found: 1241.849.

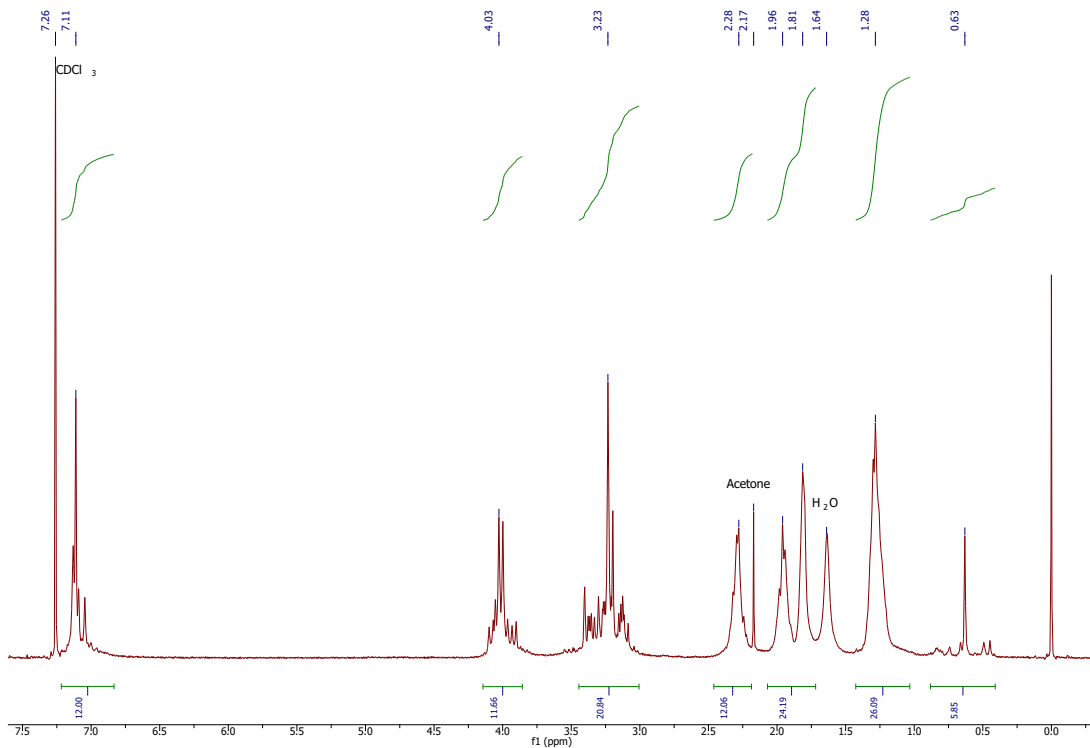


Fig. S35. ^1H NMR of 1AT-5FT-RCC3 in CDCl_3 at 25 °C.

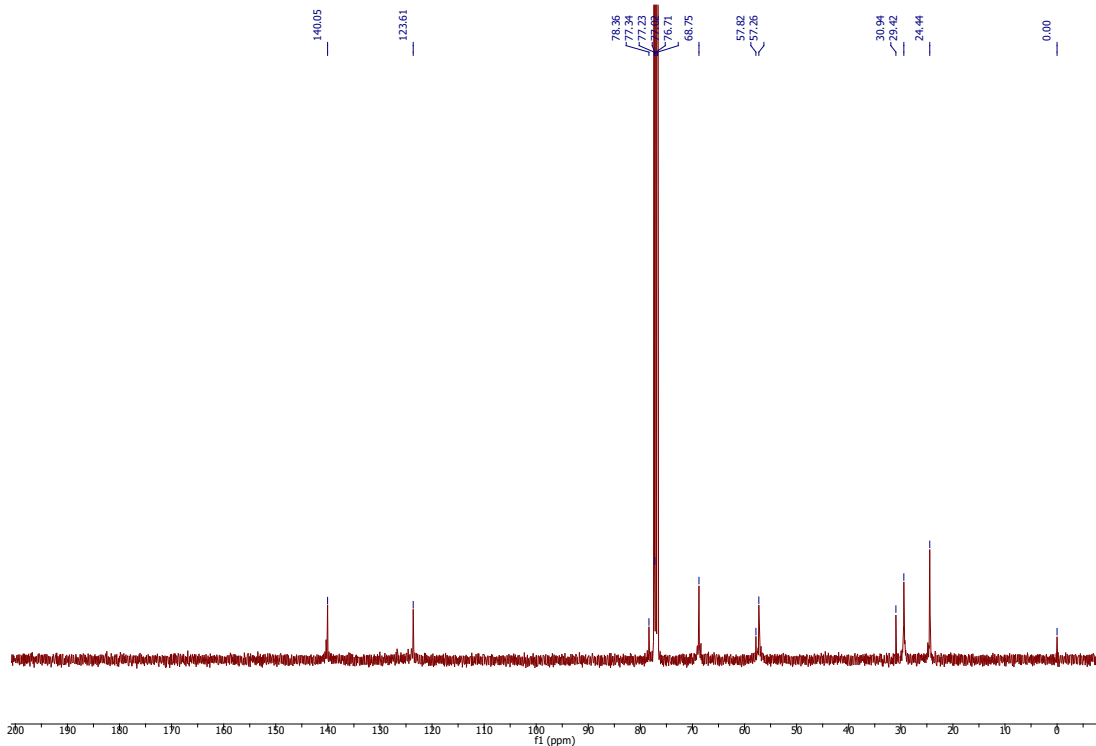


Fig. S36. ^{13}C NMR of **1AT-5FT-RCC3** in CDCl_3 at 25°C .

Synthesis of 5FT-RCC3. **1AT-5FT-RCC3** (100 mg, 0.081 mmol) was dissolved in a 20 mL mixture of CHCl_3 :MeOH (1:1, v:v). One drop of water was added and the mixture was stirred vigorously at room temperature for 12 hours. **5FT-RCC3** (91 mg, 94.0 %), was isolated as a white solid after removing the solvent under reduced pressure followed by drying under dynamic vacuum at 60 °C . ^1H NMR (CDCl_3 , 400 MHz) δ 7.55–6.75 (m, 12H, -ArH), 4.16–2.95 (m, 24H, -ArCH₂ and 10 H, -NCH₂N-), 2.50–0.85 (m, 12H, CH on cyclohexane and 48H, CH₂ on cyclohexane). ^{13}C NMR (CDCl_3 , 100 MHz): δ 140.1, 123.6, 78.4, 68.8, 57.3, 29.4, 24.4 ppm. IR (KBr pellet, ν) 2923 (s), 2854 (m), 1668 (w), 1605 (w), 1447 (m), 1349 (w), 1336 (m), 1313 (w), 1292 (w), 1215 (w), 1184 (m), 1121(w), 1066 (w), 1039 (w), 1006 (m), 950 (w), 908 (m), 858 (w), 835 (m), 749 (s), 684 (w), 666 (w) cm^{-1} . MS (ES+) 1201.8 ([M+H]⁺). Accurate mass calculated for $[\text{C}_{77}\text{H}_{109}\text{N}_{12}]^+$: 1201.813. Found: 1201.890.

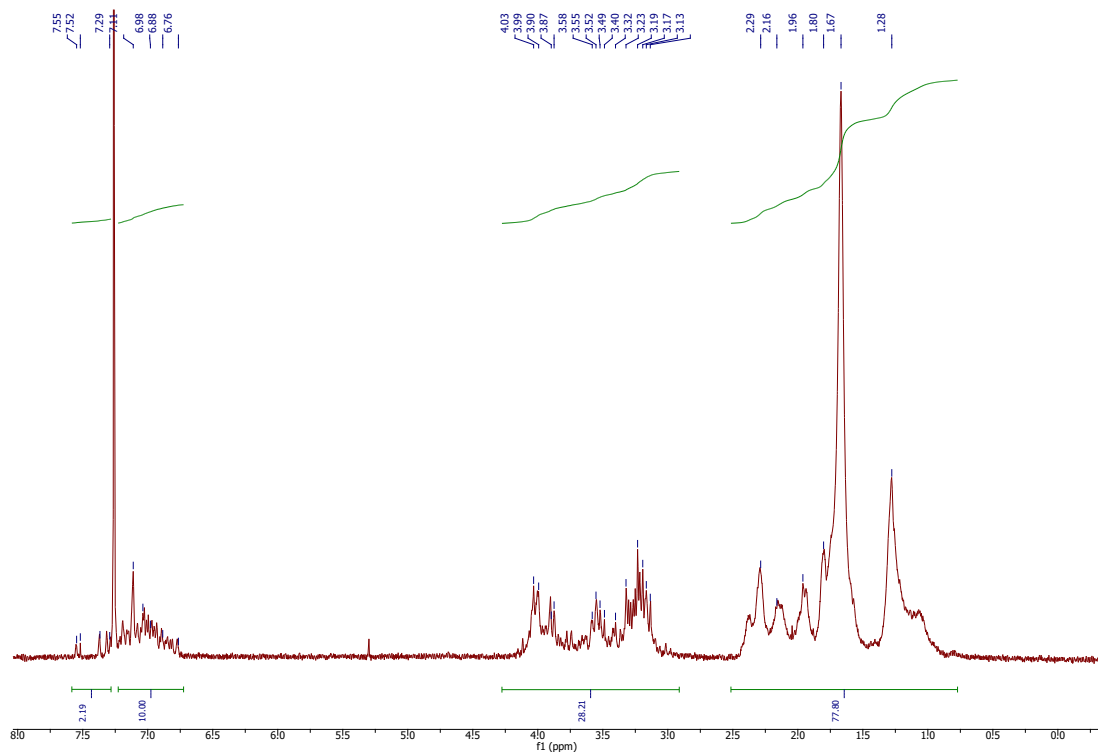


Fig. S37. ^1H NMR of **5FT-RCC3** in CDCl_3 at 25 °C.

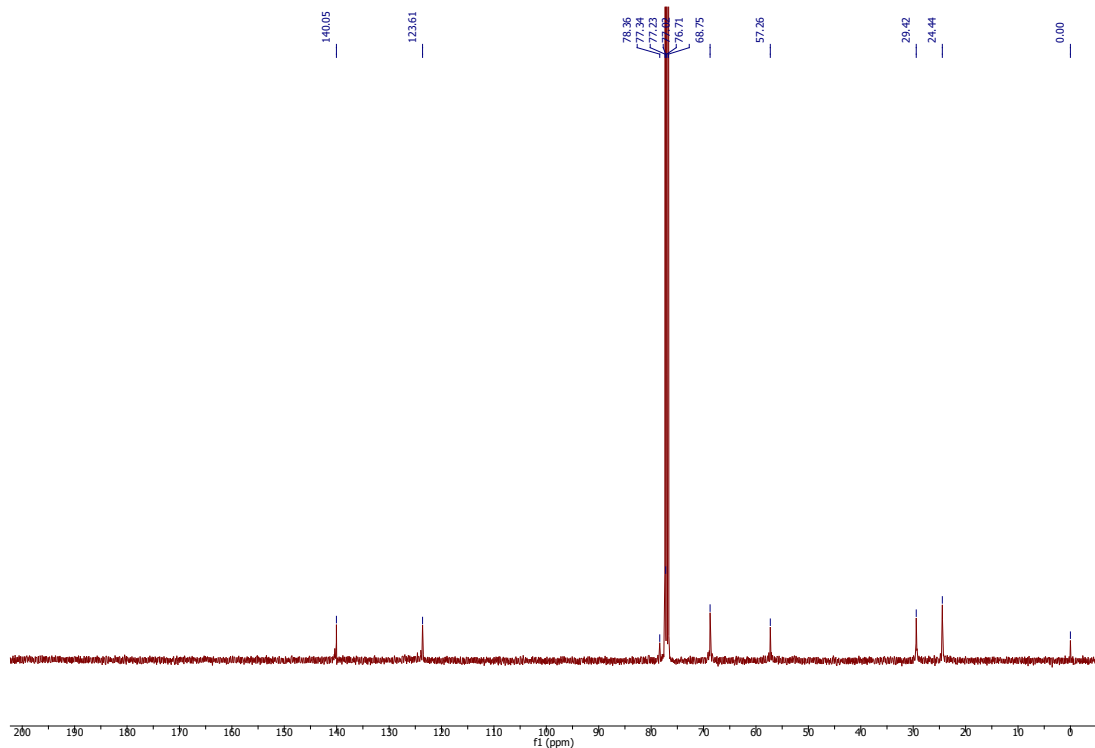


Fig. S38. ¹³C NMR of **5FT-RCC3** in CDCl_3 at 25 °C.

Synthesis of 1ET-5FT-RCC3. Ethanal (acetaldehyde 15.7 mg, 0.36 mmol) was dissolved in 10 mL CHCl₃ / MeOH (50: 50, v: v) mixture and stirred at 0 °C. **5FT-RCC3** (128 mg, 0.11 mmol) in 20 mL CHCl₃ / MeOH (50: 50, v: v) was added to the above solution at 0 °C. A white precipitate gradually appeared after this reaction mixture was stirred at room temperature. **1ET-5FT-RCC3** (126 mg, 96.3 %) was isolated as a white solid after the removal of the reaction solvents under vacuum. ¹H NMR (CDCl₃, 400 MHz) δ 7.50 – 6.99 (m, 12H, -ArH), 4.05 – 3.95 (m, 12H, -ArCH₂), 3.54–3.16 (m, 12H, -ArCH₂; 10 H, -NCH₂N- and 1H, -N₂CHCH₃-), 2.10–2.40 (m, 12H, CH on cyclohexane), 2.15–1.75 (m, 24H, CH₂ on cyclohexane), 1.40–1.10 (m, 24H, CH₂ on cyclohexane), 0.86 (m, 3H, CH₃) ppm; ¹³C NMR (CDCl₃, 100 MHz): δ 140.0, 123.6, 78.2, 68.7, 57.3, 30.9, 29.4, 24.4 ppm. IR (KBr pellet, ν) 2925 (s), 2857 (s), 2798 (w), 1606 (m), 1436 (s), 1349 (w), 1336 (s), 1313 (w), 1293 (m), 1218 (w), 1190 (m), 1122 (m), 1094 (w), 1066 (w), 1039 (w), 1006 (m), 953 (w), 908 (m), 859 (m), 836 (m), 753 (w), 685 (m) cm⁻¹. MS (ES+) 1227.9 ([M+H]⁺). Accurate mass calculated for [C₇₉H₁₁₁N₁₂]⁺: 1227.905. Found: 1227.837.

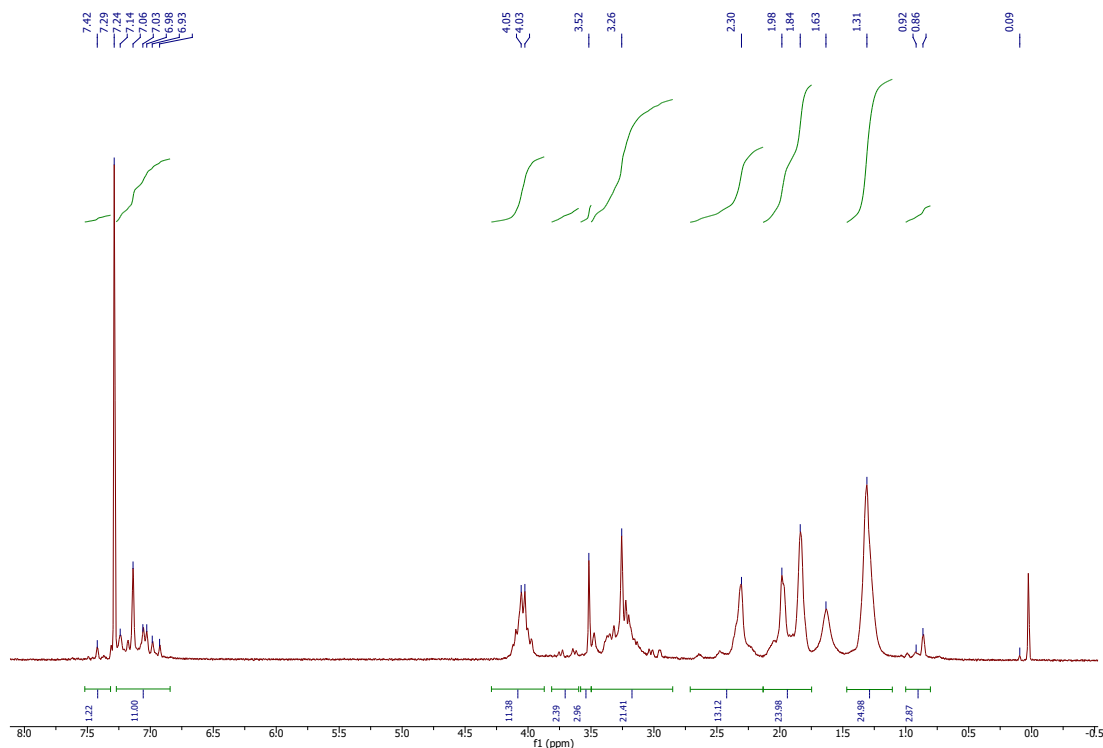


Fig. S39. ¹H NMR of **1ET-5FT-RCC3** in CDCl₃ at 25 °C.

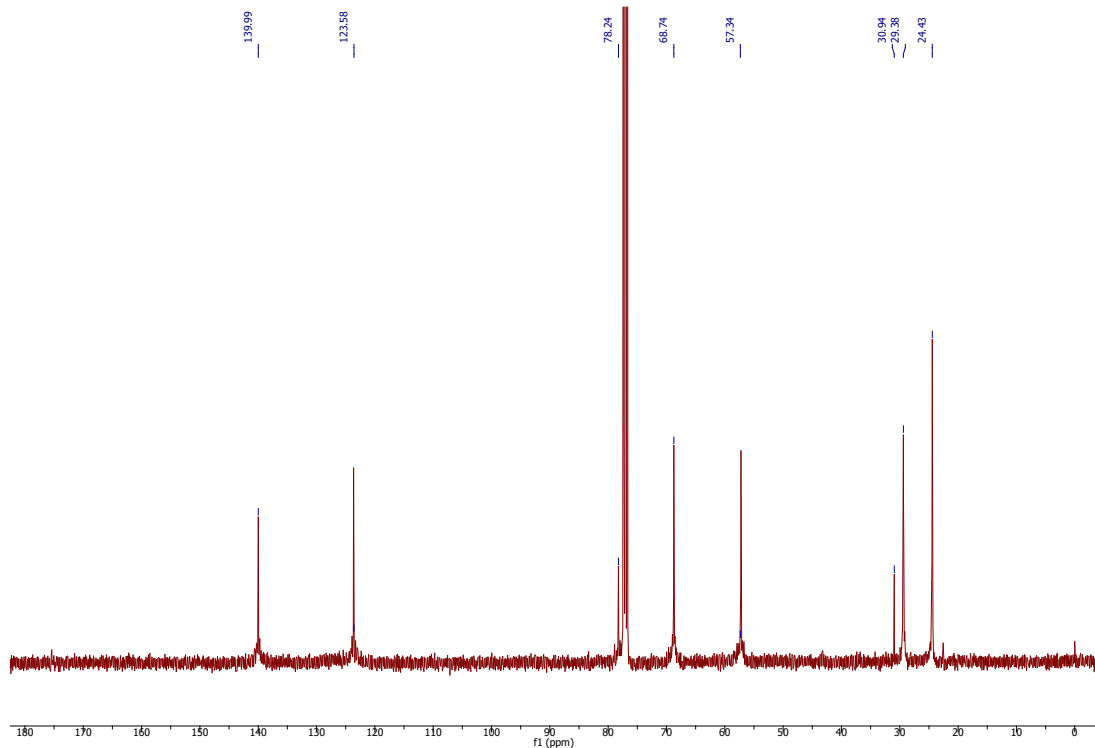


Fig. S40. ¹³C NMR of **1ET-5FT-RCC3** in CDCl₃ at 25 °C.

Synthesis of 1PT-5FT-RCC3. Propionaldehyde (5.0 mg, 0.09 mmol) was dissolved in 5 mL CHCl₃ / MeOH (50: 50, v: v) mixture and stirred at 0 °C. **5FT-RCC3** (50.0 mg, 0.04 mmol) in 10 mL CHCl₃ / MeOH (50: 50, v: v) was added to the above solution at 0 °C. A white precipitate gradually appeared after the mixture was stirred at room temperature. **1PT-5FT-RCC3** (49 mg, 94.8 %), a white solid, was recovered after removal of solvents and being dried under vacuum. ¹H NMR (CDCl₃, 400 MHz) δ 7.50–6.98 (m, 12H, -ArH), 4.25–3.75 (m, 12H, -ArCH₂), 3.49–3.15 (m, 12H, -ArCH₂ ; 10H, -NCH₂N- and 1H, -N₂CHCH₂CH₃-), 2.50 –1.50 (m, 12H, CH on cyclohexane; m, 24H, CH₂ on cyclohexane), 1.40–1.01 (m, 24H, CH₂ on cyclohexane), 0.88 (m, 5H, CH₂CH₃) ppm; ¹³C NMR (CDCl₃, 100 MHz): δ 140.0, 123.6, 78.2, 68.7, 57.3, 30.9, 29.4, 24.4 ppm. MS (ES+) 1241.9 ([M+H]⁺). Accurate mass calculated for [C₈₀H₁₁₃N₁₂]⁺: 1241.921. Found: 1241.850.

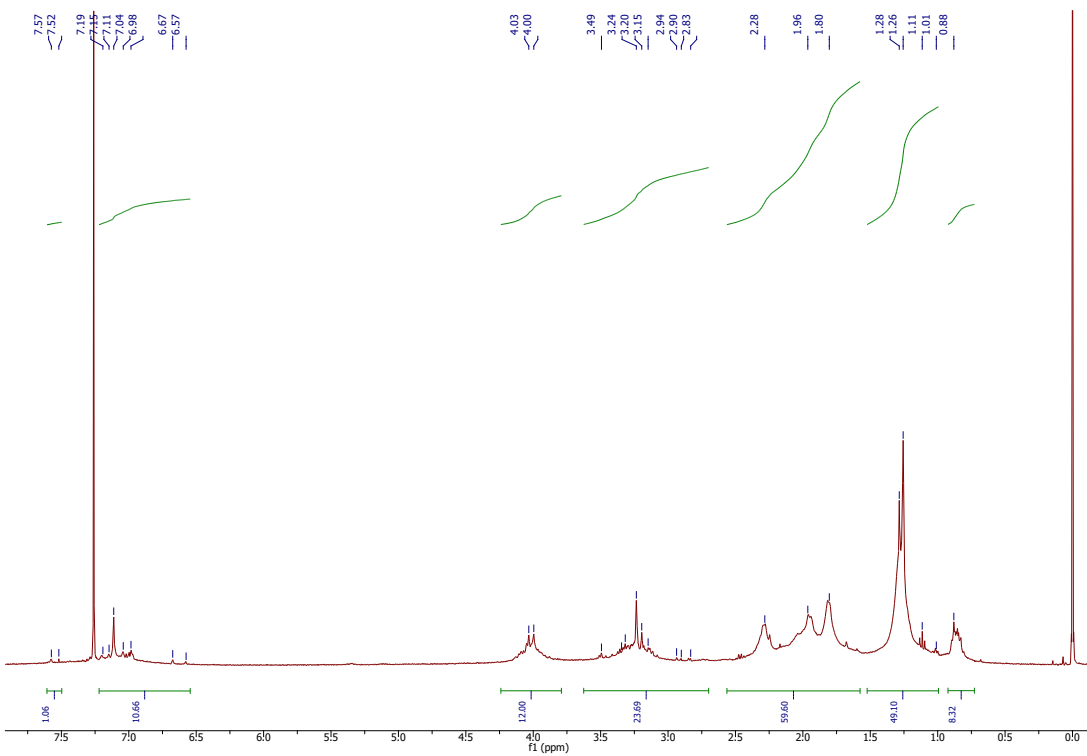


Fig. S41. ^1H NMR of **1PT-5FT-RCC3** in CDCl_3 at 25 °C.

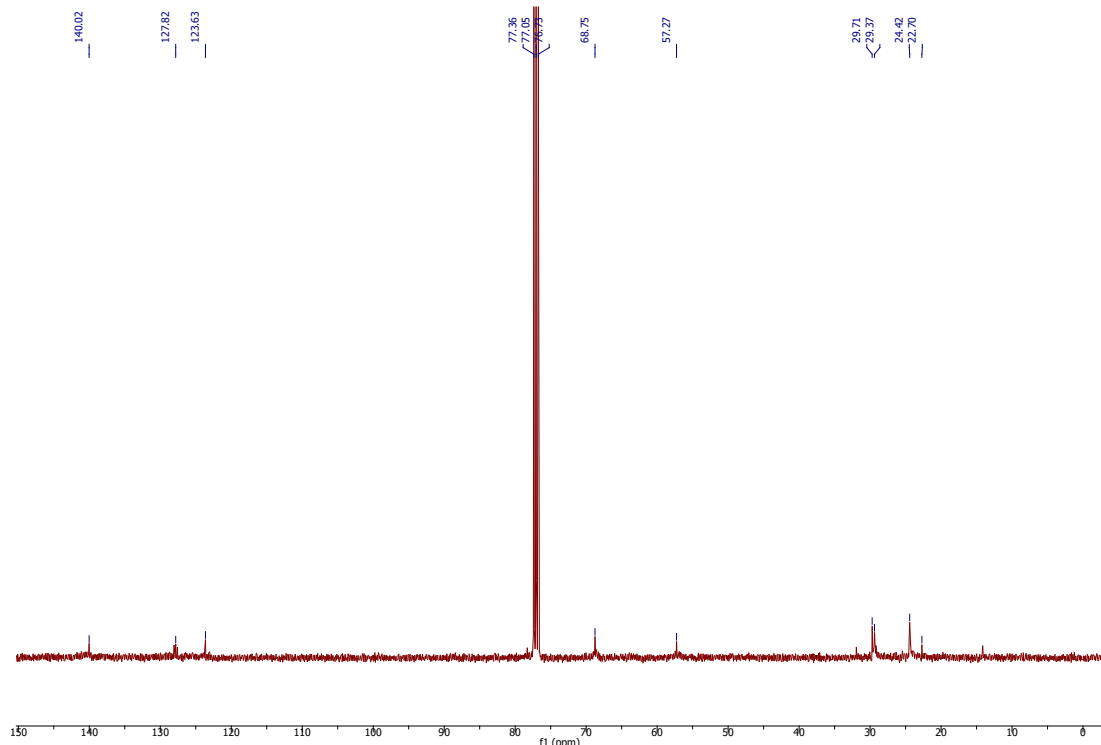


Fig. S42. ¹³C NMR of **1PT-5FT-RCC3** in CDCl₃ at 25 °C.

Synthesis of 6ET-RCC3. Acetaldehyde (200 mg, 4.55 mmol) was dissolved in MeOH (10 mL) and this solution was stirred at 0 °C. **RCC3** (500 mg, 0.438 mmol) in MeOH (20 mL) was added into the above solution. A white precipitate appeared upon addition of **RCC3**. The reaction was stirred for a further 2 h at room temperature. The precipitate was collected by filtration. **6ET-RCC3** (472 mg, 83.0 %) was obtained after washing the precipitate with MeOH (3×10 mL) and drying the product under vacuum. ^1H NMR (CDCl_3 , 400 MHz) δ 7.50–6.74 (m, 12H, -ArH), 4.23–3.05 (m, 6H, -NCHCH₃N and m, 24H, -NCH₂Ar-), 2.75–2.15 (m, 12H, CH₂ on cyclohexane), 2.10–1.75 (m, 24H, CH₂ on cyclohexane), 1.47–1.12 (m, 24H, CH₂ on cyclohexane), 0.50–0.15 (m, 18H, CH₃) ppm; ^{13}C NMR (CDCl_3 , 100 MHz): δ 140.4, 128.2, 126.6, 125.7, 123.1, 79.7, 69.4, 65.7, 52.4, 29.5, 29.4, 24.7, 20.5, 18.0 ppm. MS (ES+) 1296.9759 ([M+H]⁺). Accurate mass calculated for [C₈₄H₁₂₁N₁₂]⁺: 1297.9837. Found: 1297.9727.

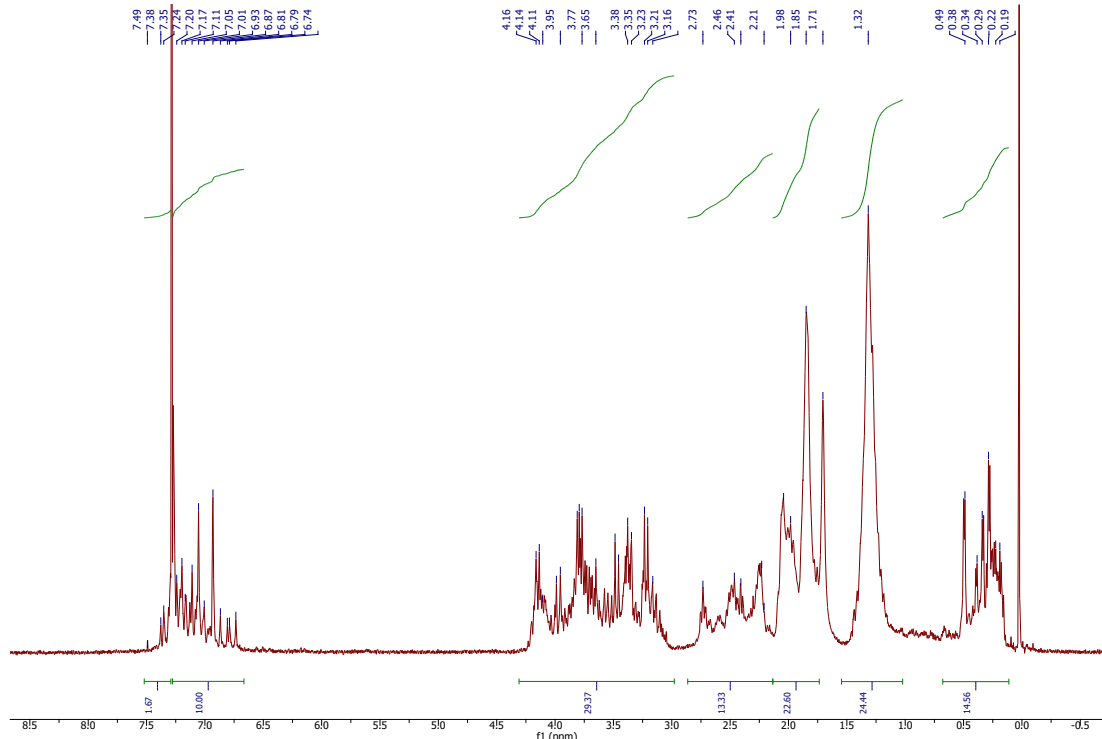


Fig. S43. ^1H NMR of **6ET-RCC3** in CDCl_3 at 25 °C.

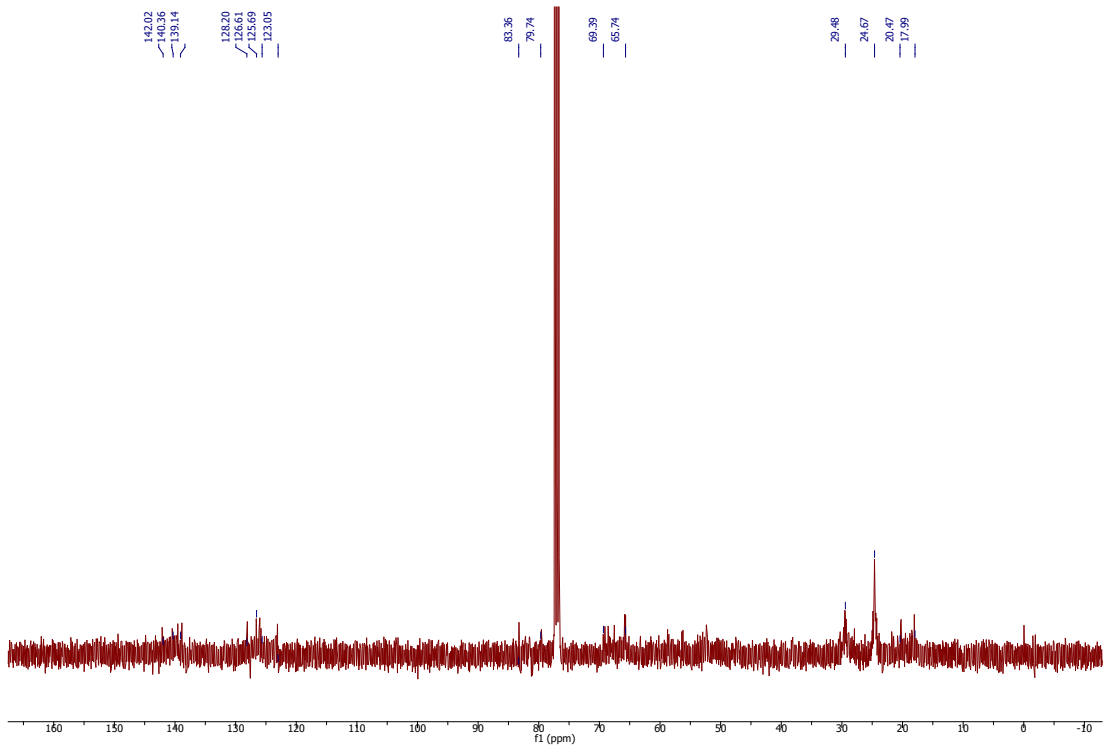


Fig. S44. ^{13}C NMR of **6ET-RCC3** in CDCl_3 at 25 °C.

References and Notes

1. H. K. Rae, “Selecting heavy water processes” in *Separation of Hydrogen Isotopes* (Symposium Series, ACS, 1978), vol. 68, chap. 1, pp. 1–26.
2. G. M. Keyser, D. B. McConnell, N. Anyas-Weiss, P. Kirkby, “Heavy Water Distillation” in *Separation of Hydrogen Isotopes* (ACS, 1978), vol. 68, pp. 126–133.
3. H. Tanaka, D. Noguchi, A. Yuzawa, T. Kodaira, H. Kanoh, K. Kaneko, Quantum effects on hydrogen isotopes adsorption in nanopores. *J. Low Temp. Phys.* **157**, 352–373 (2009). [doi:10.1007/s10909-009-9917-8](https://doi.org/10.1007/s10909-009-9917-8)
4. H. Oh, M. Hirscher, Quantum sieving for separation of hydrogen isotopes using MOFs. *Eur. J. Inorg. Chem.* **2016**, 4278–4289 (2016). [doi:10.1002/ejic.201600253](https://doi.org/10.1002/ejic.201600253)
5. J. J. Beenakker, V. D. Borman, S. Yu. Krylov, Molecular-transport in subnanometer pores: Zero-point energy, reduced dimensionality and quantum sieving. *Chem. Phys. Lett.* **232**, 379–382 (1995). [doi:10.1016/0009-2614\(94\)01372-3](https://doi.org/10.1016/0009-2614(94)01372-3)
6. J. Teufel, H. Oh, M. Hirscher, M. Wahiduzzaman, L. Zhechkov, A. Kuc, T. Heine, D. Denysenko, D. Volkmer, MFU-4—A metal-organic framework for highly effective H₍₂₎/D₍₂₎ separation. *Adv. Mater.* **25**, 635–639 (2013). [doi:10.1002/adma.201203383](https://doi.org/10.1002/adma.201203383) [Medline](#)
7. K. Adil, Y. Belmabkhout, R. S. Pillai, A. Cadiou, P. M. Bhatt, A. H. Assen, G. Maurin, M. Eddaoudi, Gas/vapour separation using ultra-microporous metal-organic frameworks: Insights into the structure/separation relationship. *Chem. Soc. Rev.* **46**, 3402–3430 (2017). [doi:10.1039/C7CS00153C](https://doi.org/10.1039/C7CS00153C) [Medline](#)
8. J.-Y. Kim, H. Oh, H.-R. Moon, Hydrogen isotope separation in confined nanospaces: Carbons, zeolites, metal–organic frameworks, and covalent organic frameworks. *Adv. Mater.* **31**, e1805293 (2019). [doi:10.1002/adma.201805293](https://doi.org/10.1002/adma.201805293) [Medline](#)
9. L. M. Robeson, The upper bound revisited. *J. Membr. Sci.* **320**, 390–400 (2008). [doi:10.1016/j.memsci.2008.04.030](https://doi.org/10.1016/j.memsci.2008.04.030)
10. Z. R. Herm, B. M. Wiers, J. A. Mason, J. M. van Baten, M. R. Hudson, P. Zajdel, C. M. Brown, N. Masciocchi, R. Krishna, J. R. Long, Separation of hexane isomers in a metal-organic framework with triangular channels. *Science* **340**, 960–964 (2013). [doi:10.1126/science.1234071](https://doi.org/10.1126/science.1234071) [Medline](#)
11. A. Cadiou, K. Adil, P. M. Bhatt, Y. Belmabkhout, M. Eddaoudi, A metal-organic framework-based splitter for separating propylene from propane. *Science* **353**, 137–140 (2016). [doi:10.1126/science.aaf6323](https://doi.org/10.1126/science.aaf6323) [Medline](#)
12. N. B. McKeown, P. M. Budd, Polymers of intrinsic microporosity (PIMs): Organic materials for membrane separations, heterogeneous catalysis and hydrogen storage. *Chem. Soc. Rev.* **35**, 675–683 (2006). [doi:10.1039/b600349d](https://doi.org/10.1039/b600349d) [Medline](#)
13. P. Kowalczyk, A. P. Terzyk, P. A. Gauden, S. Furmaniak, K. Kaneko, T. F. Miller 3rd, Nuclear quantum effects in the layering and diffusion of hydrogen isotopes in carbon nanotubes. *J. Phys. Chem. Lett.* **6**, 3367–3372 (2015). [doi:10.1021/acs.jpclett.5b01545](https://doi.org/10.1021/acs.jpclett.5b01545) [Medline](#)

14. G. Garberoglio, M. M. DeKlavon, J. K. Johnson, Quantum sieving in single-walled carbon nanotubes: Effect of interaction potential and rotational-translational coupling. *J. Phys. Chem. B* **110**, 1733–1741 (2006). [doi:10.1021/jp054511p](https://doi.org/10.1021/jp054511p) [Medline](#)
15. Q. Wang, S. R. Challa, D. S. Sholl, J. K. Johnson, Quantum sieving in carbon nanotubes and zeolites. *Phys. Rev. Lett.* **82**, 956–959 (1999). [doi:10.1103/PhysRevLett.82.956](https://doi.org/10.1103/PhysRevLett.82.956)
16. R. Xiong, R. Balderas-Xicohténcatl, L. Zhang, P. Li, Y. Yao, G. Sang, C. Chen, T. Tang, D. Luo, M. Hirscher, Thermodynamics, kinetics and selectivity of H₂ and D₂ on zeolite 5A below 77K. *Microporous Mesoporous Mater.* **264**, 22–27 (2018). [doi:10.1016/j.micromeso.2017.12.035](https://doi.org/10.1016/j.micromeso.2017.12.035)
17. M. Giraudet, I. Bezverkhyy, G. Weber, C. Dirand, M. Macaud, J.-P. Bellat, D₂/H₂ adsorption selectivity on FAU zeolites at 77.4 K: Influence of Si/Al ratio and cationic composition. *Microporous Mesoporous Mater.* **270**, 211–219 (2018). [doi:10.1016/j.micromeso.2018.05.026](https://doi.org/10.1016/j.micromeso.2018.05.026)
18. H. Oh, I. Savchenko, A. Mavrandonakis, T. Heine, M. Hirscher, Highly effective hydrogen isotope separation in nanoporous metal-organic frameworks with open metal sites: Direct measurement and theoretical analysis. *ACS Nano* **8**, 761–770 (2014). [doi:10.1021/nn405420t](https://doi.org/10.1021/nn405420t) [Medline](#)
19. B. Chen, X. Zhao, A. Putkham, K. Hong, E. B. Lobkovsky, E. J. Hurtado, A. J. Fletcher, K. M. Thomas, Surface interactions and quantum kinetic molecular sieving for H₂ and D₂ adsorption on a mixed metal-organic framework material. *J. Am. Chem. Soc.* **130**, 6411–6423 (2008). [doi:10.1021/ja710144k](https://doi.org/10.1021/ja710144k) [Medline](#)
20. H. Oh, K.-S. Park, S. B. Kalidindi, R. A. Fischer, M. Hirscher, Quantum cryo-sieving for hydrogen isotope separation in microporous frameworks: An experimental study on the correlation between effective quantum sieving and pore size. *J. Mater. Chem. A* **1**, 3244–3248 (2013). [doi:10.1039/c3ta01544k](https://doi.org/10.1039/c3ta01544k)
21. M. Lozada-Hidalgo, S. Hu, O. Marshall, A. Mishchenko, A. N. Grigorenko, R. A. W. Dryfe, B. Radha, I. V. Grigorieva, A. K. Geim, Sieving hydrogen isotopes through two-dimensional crystals. *Science* **351**, 68–70 (2016). [doi:10.1126/science.aac9726](https://doi.org/10.1126/science.aac9726) [Medline](#)
22. I. Savchenko, A. Mavrandonakis, T. Heine, H. Oh, J. Teufel, M. Hirscher, Hydrogen isotope separation in metal-organic frameworks: Kinetic or chemical affinity quantum-sieving? *Microporous Mesoporous Mater.* **216**, 133–137 (2015). [doi:10.1016/j.micromeso.2015.03.017](https://doi.org/10.1016/j.micromeso.2015.03.017)
23. H. Deng, S. Grunder, K. E. Cordova, C. Valente, H. Furukawa, M. Hmadeh, F. Gándara, A. C. Whalley, Z. Liu, S. Asahina, H. Kazumori, M. O’Keeffe, O. Terasaki, J. F. Stoddart, O. M. Yaghi, Large-pore apertures in a series of metal-organic frameworks. *Science* **336**, 1018–1023 (2012). [doi:10.1126/science.1220131](https://doi.org/10.1126/science.1220131) [Medline](#)
24. T. Tozawa, J. T. A. Jones, S. I. Swamy, S. Jiang, D. J. Adams, S. Shakespeare, R. Clowes, D. Bradshaw, T. Hasell, S. Y. Chong, C. Tang, S. Thompson, J. Parker, A. Trewin, J. Bacsa, A. M. Z. Slawin, A. Steiner, A. I. Cooper, Porous organic cages. *Nat. Mater.* **8**, 973–978 (2009). [doi:10.1038/nmat2545](https://doi.org/10.1038/nmat2545) [Medline](#)
25. T. Hasell, A. I. Cooper, Porous organic cages: Soluble, modular and molecular pores. *Nat. Rev. Mater.* **1**, 16053 (2016). [doi:10.1038/natrevmats.2016.53](https://doi.org/10.1038/natrevmats.2016.53)

26. T. Mitra, K. E. Jelfs, M. Schmidtmann, A. Ahmed, S. Y. Chong, D. J. Adams, A. I. Cooper, Molecular shape sorting using molecular organic cages. *Nat. Chem.* **5**, 276–281 (2013). [doi:10.1038/nchem.1550](https://doi.org/10.1038/nchem.1550) [Medline](#)
27. L. Chen, P. S. Reiss, S. Y. Chong, D. Holden, K. E. Jelfs, T. Hasell, M. A. Little, A. Kewley, M. E. Briggs, A. Stephenson, K. M. Thomas, J. A. Armstrong, J. Bell, J. Busto, R. Noel, J. Liu, D. M. Strachan, P. K. Thallapally, A. I. Cooper, Separation of rare gases and chiral molecules by selective binding in porous organic cages. *Nat. Mater.* **13**, 954–960 (2014). [doi:10.1038/nmat4035](https://doi.org/10.1038/nmat4035) [Medline](#)
28. M. W. Schneider, I. M. Oppel, A. Griffin, M. Mastalerz, Post-modification of the interior of porous shape-persistent organic cage compounds. *Angew. Chem. Int. Ed.* **52**, 3611–3615 (2013). [doi:10.1002/anie.201208156](https://doi.org/10.1002/anie.201208156) [Medline](#)
29. M. Liu, M. A. Little, K. E. Jelfs, J. T. A. Jones, M. Schmidtmann, S. Y. Chong, T. Hasell, A. I. Cooper, Acid- and base-stable porous organic cages: Shape persistence and pH stability via post-synthetic “tying” of a flexible amine cage. *J. Am. Chem. Soc.* **136**, 7583–7586 (2014). [doi:10.1021/ja503223j](https://doi.org/10.1021/ja503223j) [Medline](#)
30. T. Hasell, J. L. Culshaw, S. Y. Chong, M. Schmidtmann, M. A. Little, K. E. Jelfs, E. O. Pyzer-Knapp, H. Shepherd, D. J. Adams, G. M. Day, A. I. Cooper, Controlling the crystallization of porous organic cages: Molecular analogs of isoreticular frameworks using shape-specific directing solvents. *J. Am. Chem. Soc.* **136**, 1438–1448 (2014). [doi:10.1021/ja409594s](https://doi.org/10.1021/ja409594s) [Medline](#)
31. D. Banerjee, A. J. Cairns, J. Liu, R. K. Motkuri, S. K. Nune, C. A. Fernandez, R. Krishna, D. M. Strachan, P. K. Thallapally, Potential of metal-organic frameworks for separation of xenon and krypton. *Acc. Chem. Res.* **48**, 211–219 (2015). [doi:10.1021/ar5003126](https://doi.org/10.1021/ar5003126) [Medline](#)
32. C. A. Fernandez, J. Liu, P. K. Thallapally, D. M. Strachan, Switching Kr/Xe selectivity with temperature in a metal-organic framework. *J. Am. Chem. Soc.* **134**, 9046–9049 (2012). [doi:10.1021/ja302071t](https://doi.org/10.1021/ja302071t) [Medline](#)
33. D. Noguchi, H. Tanaka, A. Kondo, H. Kajiro, H. Noguchi, T. Ohba, H. Kanoh, K. Kaneko, Quantum sieving effect of three-dimensional Cu-based organic framework for H₂ and D₂. *J. Am. Chem. Soc.* **130**, 6367–6372 (2008). [doi:10.1021/ja077469f](https://doi.org/10.1021/ja077469f) [Medline](#)
34. J. T. A. Jones, T. Hasell, X. Wu, J. Bacsa, K. E. Jelfs, M. Schmidtmann, S. Y. Chong, D. J. Adams, A. Trewin, F. Schiffman, F. Cora, B. Slater, A. Steiner, G. M. Day, A. I. Cooper, Modular and predictable assembly of porous organic molecular crystals. *Nature* **474**, 367–371 (2011). [doi:10.1038/nature10125](https://doi.org/10.1038/nature10125) [Medline](#)
35. S. A. FitzGerald, C. J. Pierce, J. L. C. Rowsell, E. D. Bloch, J. A. Mason, Highly selective quantum sieving of D₂ from H₂ by a metal-organic framework as determined by gas manometry and infrared spectroscopy. *J. Am. Chem. Soc.* **135**, 9458–9464 (2013). [doi:10.1021/ja402103u](https://doi.org/10.1021/ja402103u) [Medline](#)
36. B. Xiao, P. S. Wheatley, X. Zhao, A. J. Fletcher, S. Fox, A. G. Rossi, I. L. Megson, S. Bordiga, L. Regli, K. M. Thomas, R. E. Morris, High-capacity hydrogen and nitric oxide adsorption and storage in a metal-organic framework. *J. Am. Chem. Soc.* **129**, 1203–1209 (2007). [doi:10.1021/ja066098k](https://doi.org/10.1021/ja066098k) [Medline](#)

37. L. M. Sesé, Feynman-Hibbs potentials and path integrals for quantum Lennard-Jones systems: Theory and Monte Carlo simulations. *Mol. Phys.* **85**, 931–947 (1995). [doi:10.1080/00268979500101571](https://doi.org/10.1080/00268979500101571)
38. S. Yang, L. Chen, D. Holden, R. Wang, Y. Cheng, M. Wells, A. I. Cooper, L. Ding, Understanding the effect of host flexibility on the adsorption of CH₄, CO₂ and SF₆ in porous organic cages. *Kristallogr. Cryst. Mater.* **234**, 547–555 (2019). [doi:10.1515/zkri-2018-2150](https://doi.org/10.1515/zkri-2018-2150)
39. M. Mastalerz, M. W. Schneider, I. M. Oppel, O. Presly, A salicylbisimine cage compound with high surface area and selective CO₂/CH₄ adsorption. *Angew. Chem. Int. Ed.* **50**, 1046–1051 (2011). [doi:10.1002/anie.201005301](https://doi.org/10.1002/anie.201005301) Medline
40. A. I. Cooper, Molecular organic crystals: From barely porous to really porous. *Angew. Chem. Int. Ed.* **51**, 7892–7894 (2012). [doi:10.1002/anie.201203117](https://doi.org/10.1002/anie.201203117) Medline
41. G. Zhang, O. Presly, F. White, I. M. Oppel, M. Mastalerz, A permanent mesoporous organic cage with an exceptionally high surface area. *Angew. Chem. Int. Ed.* **53**, 1516–1520 (2014). [doi:10.1002/anie.201308924](https://doi.org/10.1002/anie.201308924) Medline
42. A. Pulido, L. Chen, T. Kaczorowski, D. Holden, M. A. Little, S. Y. Chong, B. J. Slater, D. P. McMahon, B. Bonillo, C. J. Stackhouse, A. Stephenson, C. M. Kane, R. Clowes, T. Hasell, A. I. Cooper, G. M. Day, Functional materials discovery using energy-structure-function maps. *Nature* **543**, 657–664 (2017). [doi:10.1038/nature21419](https://doi.org/10.1038/nature21419) Medline
43. G. J. Kleywegt, T. A. Jones, Detection, delineation, measurement and display of cavities in macromolecular structures. *Acta Crystallogr. D* **50**, 178–185 (1994). [doi:10.1107/S0907444993011333](https://doi.org/10.1107/S0907444993011333) Medline
44. J. Teufel, “Experimental investigation of H₂/D₂ isotope separation by cryo-adsorption in metal-organic frameworks,” thesis, Universität Stuttgart (2013).
45. S. S. Mondal, A. Kreuzer, K. Behrens, G. Schütz, H.-J. Holdt, M. Hirscher, Systematic experimental study on quantum sieving of hydrogen isotopes in metal–amide–imidazolate frameworks with narrow 1–D channels. *ChemPhysChem* **20**, 1311–1315 (2019). [doi:10.1002/cphc.201900183](https://doi.org/10.1002/cphc.201900183) Medline
46. H. Oh, S. B. Kalidindi, Y. Um, S. Bureekaew, R. Schmid, R. A. Fischer, M. Hirscher, A cryogenically flexible covalent organic framework for efficient hydrogen isotope separation by quantum sieving. *Angew. Chem. Int. Ed.* **52**, 13219–13222 (2013). [doi:10.1002/anie.201307443](https://doi.org/10.1002/anie.201307443) Medline
47. L. Krause, R. Herbst-Irmer, G. M. Sheldrick, D. Stalke, Comparison of silver and molybdenum microfocus X-ray sources for single-crystal structure determination. *J. Appl. Crystallogr.* **48**, 3–10 (2015). [doi:10.1107/S1600576714022985](https://doi.org/10.1107/S1600576714022985) Medline
48. A. S. Brewster, D. G. Waterman, J. M. Parkhurst, R. J. Gildea, I. D. Young, L. J. O’Riordan, J. Yano, G. Winter, G. Evans, N. K. Sauter, Improving signal strength in serial crystallography with DIALS geometry refinement. *Acta Crystallogr. D* **74**, 877–894 (2018). [doi:10.1107/S2059798318009191](https://doi.org/10.1107/S2059798318009191) Medline
49. G. M. Sheldrick, SHELXT - integrated space-group and crystal-structure determination. *Acta Crystallogr. A* **71**, 3–8 (2015). [doi:10.1107/S2053273314026370](https://doi.org/10.1107/S2053273314026370) Medline

50. G. M. Sheldrick, Crystal structure refinement with SHELXL. *Acta Crystallogr. C* **71**, 3–8 (2015). [doi:10.1107/S2053229614024218](https://doi.org/10.1107/S2053229614024218) [Medline](#)
51. O. V. Dolomanov, L. J. Bourhis, R. J. Gildea, J. A. K. Howard, H. Puschmann, OLEX2: A complete structure solution, refinement and analysis program. *J. Appl. Cryst.* **42**, 339–341 (2009). [doi:10.1107/S0021889808042726](https://doi.org/10.1107/S0021889808042726)
52. A. G. Slater, P. S. Reiss, A. Pulido, M. A. Little, D. L. Holden, L. Chen, S. Y. Chong, B. M. Alston, R. Clowes, M. Haranczyk, M. E. Briggs, T. Hasell, G. M. Day, A. I. Cooper, Computationally-guided synthetic control over pore size in isostructural porous organic cages. *ACS Cent. Sci.* **3**, 734–742 (2017). [doi:10.1021/acscentsci.7b00145](https://doi.org/10.1021/acscentsci.7b00145) [Medline](#)
53. X.-Z. Chu, Z.-P. Cheng, Y.-J. Zhao, J.-M. Xu, M.-S. Li, L. Zhou, C.-H. Lee, Adsorption dynamics of hydrogen and deuterium in a carbon molecular sieve bed at 77 K. *Separ. Purif. Tech.* **146**, 168–175 (2015). [doi:10.1016/j.seppur.2015.03.036](https://doi.org/10.1016/j.seppur.2015.03.036)
54. K. Kotoh, M. Tanaka, Y. Nakamura, T. Sakamoto, Y. Asakura, T. Uda, T. Sugiyama, Experimental verification of hydrogen isotope separation by pressure swing adsorption. *Fus. Sci. Technol.* **54**, 411–414 (2008). [doi:10.13182/FST08-A1842](https://doi.org/10.13182/FST08-A1842)
55. X.-Z. Chu, Y.-J. Zhao, Y.-H. Kan, W.-G. Zhang, S.-Y. Zhou, Y.-P. Zhou, L. Zhou, Dynamic experiments and model of hydrogen and deuterium separation with micropore molecular sieve Y at 77 K. *Chem. Eng. J.* **152**, 428–433 (2009). [doi:10.1016/j.cej.2009.04.068](https://doi.org/10.1016/j.cej.2009.04.068)
56. X. Zhao, S. Villar-Rodil, A. J. Fletcher, K. M. Thomas, Kinetic isotope effect for H₂ and D₂ quantum molecular sieving in adsorption/desorption on porous carbon materials. *J. Phys. Chem. B* **110**, 9947–9955 (2006). [doi:10.1021/jp060748p](https://doi.org/10.1021/jp060748p) [Medline](#)
57. Y. Xing, J. Cai, L. Li, M. Yang, X. Zhao, An exceptional kinetic quantum sieving separation effect of hydrogen isotopes on commercially available carbon molecular sieves. *Phys. Chem. Chem. Phys.* **16**, 15800–15805 (2014). [doi:10.1039/C4CP00709C](https://doi.org/10.1039/C4CP00709C) [Medline](#)
58. H. Tanaka, H. Kanoh, M. Yudasaka, S. Iijima, K. Kaneko, Quantum effects on hydrogen isotope adsorption on single-wall carbon nanohorns. *J. Am. Chem. Soc.* **127**, 7511–7516 (2005). [doi:10.1021/ja0502573](https://doi.org/10.1021/ja0502573) [Medline](#)
59. D. Noguchi, Y. Hattori, C. M. Yang, Y. Tao, T. Konishi, T. Fujikawa, T. Ohkubo, Y. Nobuhara, T. Ohba, H. Tanaka, H. Kanoh, M. Yudasaka, S. Iijima, H. Sakai, M. Abe, Y. J. Kim, M. Endo, K. Kaneko, Storage function of carbon nanospaces for molecules and ions. *ECS Trans.* **11**, 63–75 (2007). [doi:10.1149/1.2783303](https://doi.org/10.1149/1.2783303)
60. D. Noguchi, H. Tanaka, T. Fujimori, H. Kagita, Y. Hattori, H. Honda, K. Urita, S. Utsumi, Z. M. Wang, T. Ohba, H. Kanoh, K. Hata, K. Kaneko, Selective D₂ adsorption enhanced by the quantum sieving effect on entangled single-wall carbon nanotubes. *J. Phys. Condens. Matter* **22**, 334207 (2010). [doi:10.1088/0953-8984/22/33/334207](https://doi.org/10.1088/0953-8984/22/33/334207) [Medline](#)
61. K. Kotoh, T. Nishikawa, Y. Kashio, Multi-component adsorption characteristics of hydrogen isotopes on synthetic zeolite 5A-type at 77.4 K. *J. Nucl. Sci. Technol.* **39**, 435–441 (2002). [doi:10.1080/18811248.2002.9715219](https://doi.org/10.1080/18811248.2002.9715219)
62. J. Salazar, S. Lectez, C. Gauvin, M. Macaud, J. P. Bellat, G. Weber, I. Bezverkhyy, J. M. Simon, Adsorption of hydrogen isotopes in the zeolite NaX: Experiments and

- simulations. *Int. J. Hydrogen Energy* **42**, 13099–13110 (2017). [doi:10.1016/j.ijhydene.2017.03.222](https://doi.org/10.1016/j.ijhydene.2017.03.222)
63. X.-Z. Chu, Y.-P. Zhou, Y.-Z. Zhang, W. Su, Y. Sun, L. Zhou, Adsorption of hydrogen isotopes on micro- and mesoporous adsorbents with orderly structure. *J. Phys. Chem. B* **110**, 22596–22600 (2006). [doi:10.1021/jp064745o](https://doi.org/10.1021/jp064745o) [Medline](#)
64. K. Kotoh, K. Kudo, Multi-component adsorption behavior of hydrogen isotopes on zeolite 5A and 13X at 77.4 K. *Fus. Sci. Technol.* **48**, 148–151 (2005). [doi:10.13182/FST05-A900](https://doi.org/10.13182/FST05-A900)
65. A. Sharma, K. V. Lawler, J. J. Wolffis, C. T. Eckdahl, C. S. McDonald, J. L. C. Rowsell, S. A. FitzGerald, P. M. Forster, Hydrogen uptake on coordinatively unsaturated metal sites in VSB-5: Strong binding affinity leading to high-temperature D₂/H₂ selectivity. *Langmuir* **33**, 14586–14591 (2017). [doi:10.1021/acs.langmuir.7b03580](https://doi.org/10.1021/acs.langmuir.7b03580) [Medline](#)
66. J. Jia, X. Lin, C. Wilson, A. J. Blake, N. R. Champness, P. Hubberstey, G. Walker, E. J. Cussen, M. Schröder, Twelve-connected porous metal-organic frameworks with high H₍₂₎ adsorption. *Chem. Commun.* 2007, 840–842 (2007). [doi:10.1039/B614254K](https://doi.org/10.1039/B614254K) [Medline](#)
67. X. Lin, J. Jia, X. Zhao, K. M. Thomas, A. J. Blake, G. S. Walker, N. R. Champness, P. Hubberstey, M. Schröder, High H₂ adsorption by coordination-framework materials. *Angew. Chem. Int. Ed.* **45**, 7358–7364 (2006). [doi:10.1002/anie.200601991](https://doi.org/10.1002/anie.200601991) [Medline](#)
68. K. Kotoh, K. Kimura, Y. Nakamura, K. Kudo, Hydrogen isotope separation using molecular sieve of synthetic zeolite 3A. *Fus. Sci. Technol.* **54**, 419–422 (2008). [doi:10.13182/FST08-A1844](https://doi.org/10.13182/FST08-A1844)
69. S. Niimura, T. Fujimori, D. Minami, Y. Hattori, L. Abrams, D. Corbin, K. Hata, K. Kaneko, Dynamic quantum molecular sieving separation of D₂ from H₂-D₂ mixture with nanoporous materials. *J. Am. Chem. Soc.* **134**, 18483–18486 (2012). [doi:10.1021/ja305809u](https://doi.org/10.1021/ja305809u) [Medline](#)
70. T. F. Willems, C. Rycroft, M. Kazi, J. C. Meza, M. Haranczyk, Algorithms and tools for high-throughput geometry-based analysis of crystalline porous materials. *Microporous Mesoporous Mater.* **149**, 134–141 (2012). [doi:10.1016/j.micromeso.2011.08.020](https://doi.org/10.1016/j.micromeso.2011.08.020)
71. W. Smith, T. R. Forester, DL_POLY_2.0: A general-purpose parallel molecular dynamics simulation package. *J. Mol. Graph.* **14**, 136–141 (1996). [doi:10.1016/S0263-7855\(96\)00043-4](https://doi.org/10.1016/S0263-7855(96)00043-4) [Medline](#)
72. D. Levesque, A. Gicquel, F. L. Darkrim, S. B. Kayiran, Monte Carlo simulations of hydrogen storage in carbon nanotubes. *J. Phys. Condens. Matter* **14**, 9285–9293 (2002). [doi:10.1088/0953-8984/14/40/318](https://doi.org/10.1088/0953-8984/14/40/318)
73. W. L. Jorgensen, D. S. Maxwell, J. Tirado-Rives, J. TiradoRives, Development and testing of the OPLS all-atom force field on conformational energetics and properties of organic liquids. *J. Am. Chem. Soc.* **118**, 11225–11236 (1996). [doi:10.1021/ja9621760](https://doi.org/10.1021/ja9621760)
74. D. Dubbeldam, S. Calero, D. E. Ellis, R. Q. Snurr, RASPA: Molecular simulation software for adsorption and diffusion in flexible nanoporous materials. *Mol. Simul.* **42**, 81–101 (2016). [doi:10.1080/08927022.2015.1010082](https://doi.org/10.1080/08927022.2015.1010082)

75. D. Dubbeldam, E. Beerdsen, S. Calero, B. Smit, Dynamically corrected transition state theory calculations of self-diffusion in anisotropic nanoporous materials. *J. Phys. Chem. B* **110**, 3164–3172 (2006). [doi:10.1021/jp0542470](https://doi.org/10.1021/jp0542470) [Medline](#)
76. M. Gaus, Q. Cui, M. Elstner, DFTB3: Extension of the self-consistent-charge density-functional tight-binding method (SCC-DFTB). *J. Chem. Theory Comput.* **7**, 931–948 (2012). [doi:10.1021/ct100684s](https://doi.org/10.1021/ct100684s) [Medline](#)
77. L. Zhechkov, T. Heine, S. Patchkovskii, G. Seifert, H. A. Duarte, An efficient a posteriori treatment for dispersion interaction in Density-Functional-Based Tight Binding. *J. Chem. Theory Comput.* **1**, 841–847 (2005). [doi:10.1021/ct050065y](https://doi.org/10.1021/ct050065y) [Medline](#)
78. M. Gaus, A. Goez, M. Elstner, Parametrization and benchmark of DFTB3 for organic Molecules. *J. Chem. Theory Comput.* **9**, 338–354 (2013). [doi:10.1021/ct300849w](https://doi.org/10.1021/ct300849w) [Medline](#)
79. J. VandeVondele, J. Hutter, Gaussian basis sets for accurate calculations on molecular systems in gas and condensed phases. *J. Chem. Phys.* **127**, 114105 (2007). [doi:10.1063/1.2770708](https://doi.org/10.1063/1.2770708) [Medline](#)
80. M. Krack, Pseudopotentials for H to Kr optimized for gradient-corrected exchange-correlation functionals. *Theor. Chem. Acc.* **114**, 145–152 (2005). [doi:10.1007/s00214-005-0655-y](https://doi.org/10.1007/s00214-005-0655-y)
81. T. Hasell, M. Miklitz, A. Stephenson, M. A. Little, S. Y. Chong, R. Clowes, L. Chen, D. Holden, G. A. Tribello, K. E. Jelfs, A. I. Cooper, Porous organic cages for sulfur hexafluoride separation. *J. Am. Chem. Soc.* **138**, 1653–1659 (2016). [doi:10.1021/jacs.5b11797](https://doi.org/10.1021/jacs.5b11797) [Medline](#)
82. M. Parrinello, A. Rahman, Study of an F center in molten KCl. *J. Chem. Phys.* **80**, 860–867 (1984). [doi:10.1063/1.446740](https://doi.org/10.1063/1.446740)
83. D. Chandler, P. G. Wolynes, Exploiting the isomorphism between quantum theory and classical statistical mechanics of polyatomic fluids. *J. Chem. Phys.* **74**, 4078–4095 (1981). [doi:10.1063/1.441588](https://doi.org/10.1063/1.441588)
84. V. I. Tikhonov, A. A. Volkov, Separation of water into its ortho and para isomers. *Science* **296**, 2363 (2002). [doi:10.1126/science.1069513](https://doi.org/10.1126/science.1069513) [Medline](#)
85. D. M. Ceperley, G. Jacucci, Calculation of exchange frequencies in bcc 3He with the path-integral Monte Carlo method. *Phys. Rev. Lett.* **58**, 1648–1651 (1987). [doi:10.1103/PhysRevLett.58.1648](https://doi.org/10.1103/PhysRevLett.58.1648) [Medline](#)
86. T. E. Markland, B. J. Berne, Unraveling quantum mechanical effects in water using isotopic fractionation. *Proc. Natl. Acad. Sci. U.S.A.* **109**, 7988–7991 (2012). [doi:10.1073/pnas.1203365109](https://doi.org/10.1073/pnas.1203365109) [Medline](#)
87. C. McBride, E. G. Noya, J. L. Aragones, M. M. Conde, C. Vega, The phase diagram of water from quantum simulations. *Phys. Chem. Chem. Phys.* **14**, 10140–10146 (2012). [doi:10.1039/c2cp40962c](https://doi.org/10.1039/c2cp40962c) [Medline](#)
88. M. Ceriotti, T. E. Markland, Efficient methods and practical guidelines for simulating isotope effects. *J. Chem. Phys.* **138**, 014112 (2013). [doi:10.1063/1.4772676](https://doi.org/10.1063/1.4772676) [Medline](#)

89. V. Kapil, M. Rossi, O. Marsalek, R. Petraglia, Y. Litman, T. Spura, B. Q. Cheng, A. Cuzzocrea, R. H. Meissner, D. M. Wilkins, B. A. Helfrech, P. Juda, S. P. Bienvenue, W. Fang, J. Kessler, I. Poltavsky, S. Vandenbrande, J. Wieme, C. Corminboef, T. D. Kuhne, D. E. Manolopoulos, T. E. Markland, J. O. Richardson, A. Tkatchenko, G. A. Tribello, V. Van Speybroeck, M. Ceriotti, i-PI 2.0: A universal force engine for advanced molecular simulations. *Comput. Phys. Commun.* **236**, 214–223 (2019). [doi:10.1016/j.cpc.2018.09.020](https://doi.org/10.1016/j.cpc.2018.09.020)
90. M. Ceriotti, D. E. Manolopoulos, Efficient first-principles calculation of the quantum kinetic energy and momentum distribution of nuclei. *Phys. Rev. Lett.* **109**, 100604 (2012). [doi:10.1103/PhysRevLett.109.100604](https://doi.org/10.1103/PhysRevLett.109.100604) [Medline](#)
91. B. Aradi, B. Hourahine, T. Frauenheim, DFTB+, a sparse matrix-based implementation of the DFTB method. *J. Phys. Chem. A* **111**, 5678–5684 (2007). [doi:10.1021/jp070186p](https://doi.org/10.1021/jp070186p) [Medline](#)
92. B. Leimkuhler, C. Matthews, Robust and efficient configurational molecular sampling via Langevin dynamics. *J. Chem. Phys.* **138**, 174102 (2013). [doi:10.1063/1.4802990](https://doi.org/10.1063/1.4802990) [Medline](#)
93. G. M. Torrie, J. P. Valleau, Nonphysical sampling distributions in Monte Carlo free-energy estimation: Umbrella sampling. *J. Comput. Phys.* **23**, 187–199 (1977). [doi:10.1016/0021-9991\(77\)90121-8](https://doi.org/10.1016/0021-9991(77)90121-8)
94. G. A. Tribello, M. Bonomi, D. Branduardi, C. Camilloni, G. Bussi, PLUMED 2: New feathers for an old bird. *Comput. Phys. Commun.* **185**, 604–613 (2014). [doi:10.1016/j.cpc.2013.09.018](https://doi.org/10.1016/j.cpc.2013.09.018)
95. A. Grossfield, WHAM: the weighted histogram analysis method, version 2.0. 9 (2013); <http://membrane.urmc.rochester.edu/content/wham>.